TOWARDS A CANFIELD JOINT FOR DEEP SPACE OPTICAL COMMUNICATION

by

KRISTINA VENEPHE COLLINS

Submitted in partial fulfillment of the requirements

For the degree of Master of Science

Thesis Adviser: Dr. Christian Zorman

Department of Electrical Engineering and Computer Science

CASE WESTERN RESERVE UNIVERSITY

January, 2019

Towards a Canfield Joint for Deep Space Optical Communication

Case Western Reserve University
Case School of Graduate Studies

We hereby approve the thesis[1] of

KRISTINA VENEPHE COLLINS

for the degree of

Master of Science

Dr. Christian Zorman

Associate Dean of Research
Case School of Engineering

Dr. Francis Merat

Professor Emeritus
Department of Electrical Engineering and Computer Science

Dr. M. Cenk Çavuşoğlu

Professor
Department of Electrical Engineering and Computer Science

Dr. Wyatt Newman

Professor
Department of Electrical Engineering and Computer Science

Dr. Daniel Raible

Professor, University of Akron
Aerospace Systems Engineering

[1]We certify that written approval has been obtained for any proprietary material contained therein.

Dedicated to my family.

Table of Contents

List of Tables

List of Figures

Acknowledgments

Credit for my completion of this work is due above all to the inimitable Alan Hylton and the indefatigable Dr. Daniel Raible, who hired me in the first place and then hired me again anyway. Dr. Stephen Canfield must naturally be acknowledged for coming up with the widget explored herein. Much of the geometric analysis is based on the work of Bob Short and Christian Bueno, without whom I would not have any inkling I could enjoy topology. Useful discussions and many cups of tea were shared with the other acolytes of the Temple of Interns: Ethan Pelagalli, Emily Walter, and Tom Gebhart, as well as with Stephanie Booth and Emily Clapper. Dr. Cenk Cavusoglu was particularly instrumental in helping me understand how to throw math at this problem and many others. Much credit is due to Ben Kaufman, who largely pioneered and perfected the LEGO Canfield model, supported me through the project, and only broke my computer once. Credit is due to Robert Wiesler for fixing my computer, and for making my code a lot better. Much of the code in question was adapted from the work of Dr. Wyatt Newman, to whom I am indebted for the introduction to ROS. Caelin Mercer is largely responsible for turning the original prototype drawings of Anthony Ganino into a SolidWorks model, and solely responsible for that model being any good. Additive manufacturing capabilities, materials, and assistance were provided by think[box], the Building 77 lab guys (Lawrence Greer, Norman Prokop and Mike Krasowski), and the staff of the LEGO Store at Beachwood Mall. Many thanks to Dr. Christian Zorman for his patience and guidance, especially his patience. Thanks also to Dr. Frank Merat for his mentorship and our many conversations over the years, and to Dr. David Kazdan for his mentorship and support. I wish to particularly acknowledge the love and support of my family; Michael, Sunniva, and William Collins. Finally, moral support was provided throughout by Jane Lindsay, Michael Peabody, Nathaniel Vishner, Rachel Boedicker, Tyler Laseter and Kellen McGee, and all of their cats. There are many others as well, but the margin is now too small for the proof.

Abstract

Towards a Canfield Joint for Deep Space Optical Communication

KRISTINA VENEPHE COLLINS

This thesis comprises work supporting the integration of a Canfield joint (carpal wrist) in the Integrated Radio and Optical Communication project at NASA Glenn Research Center. The Canfield joint is a 3 DoF (degree of freedom) parallel linkage used for pointing a range of end effectors. Several tests were devised and performed to validate an existing prototype for optical pointing requirements including field of regard, pointing resolution, and slew rate for a trajectory between Earth and Mars; these requirements were partially satisfied. A kinematic analysis of the robot is performed, including forward and inverse kinematics and preliminary singularity analysis, and the effect of altering the ratio of base and leg lengths is investigated. Designs for physical models of the Canfield joint, produced using rapid prototyping, are presented, as are computer models produced for use in Geogebra and Robot Operating System.

1 Motivation

NASA has sent space probes to every planet in the solar system and several moons, and its networks currently maintain communication with approximately 100 spacecraft. Up to 95% of data collected by these probes never finds its way to Earth.[4] This is partly a consequence of signal attenuation over vast distances, and partly a function of the finite capacity of the space communication network. For future missions,

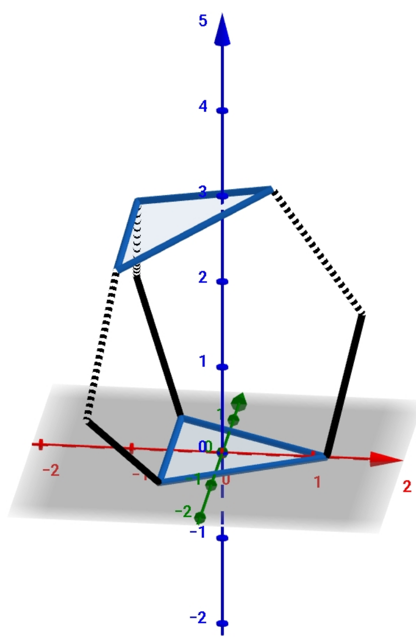

Figure 1.1. Simplified model of the Canfield with coordinate frame, approximating the revolute leg joints as a single spherical joint.

and especially for human exploration, it is imperative to construct a robust space communications infrastructure capable of higher data rates. Optical communication systems currently under development can offer a hundredfold increase in data rate at a fraction of the mass of existing radio-based systems. The successful Lunar Laser Communication Demonstration, part of NASA's Lunar Atmosphere and Dust Environment Explorer (LADEE) mission in 2013, set a downlink record of 622 megabits per second (Mbps) from spacecraft to ground. The focus of the Integrated Radio and Optical Communication Project (iROC) at NASA Glenn Research Center, through which this work was supported, is to continue this evolution by combining optical and radio frequency communication infrastructure into a single unit.

However, deep space laser communication requires high precision pointing. From Mars, the beam footprint of an X-band radar using a 3m antenna is greater than 10,000 times the projected area of the Earth, whereas an optical beam from a 30 cm antenna is on the order of 1% of the Earth's projected area.[5] Currently, there are no commercially available gimbals that can satisfy the pointing precision and articulated mass requirements for the iROC project. The Canfield joint, shown schematically in Figure 1.1, offers a potential solution for this problem, because of its reduced size, weight and power (SWaP) constraints compared to a traditional gimbal.

The Canfield joint, first proposed in 1997[6], is a parallel robotic linkage with 3 degrees of freedom (DoF), modeled on the movement of a wrist. Each of its 3 identical legs has a $\underline{R}$UR kinematic chain.[1] The linkage is actuated by three driven revolute joints at its base, which enable pointing motion in a hemispherical workspace.

[1]Per the notation in Section 2.6.1, R represents a revolute joint and U a universal joint. Driven joints are underlined.

In order to deploy the Canfield joint in an operational environment, it is necessary to ensure that the robot can be reliably controlled. If the robot enters a singular configuration (i.e., a configuration in which it loses one or more degrees of freedom), control may be compromised. Although forward and inverse kinematics solutions are already available[6], a rigorous analysis of the kinematics is required.

Another goal of using the Canfield joint in this work is to raise the technology readiness level[2] (TRL) of the linkage so it may be used for a wider range of applications. NASA has expressed interest in using it for a variety of end effectors in space applications, including pointing and tracking for solar cells and thrusters. These projects are discussed in detail in Chapter 2.

The goals of this research were threefold: First, to validate the existing NASA prototype according to the project requirements of the iROC project; second, to perform a rigorous kinematic analysis of the Canfield joint; and third, to produce computer models extensible to future use. This document is intended to serve as an engineering reference for implementing this linkage, both in integration tasks specific to iROC and in general usage. Following a literature review in Chapter 2, validation procedures and results for the existing prototype are presented in Chapter 4. A general kinematic analysis is presented in Chapter 3, which builds on existing work[6]. Physical and computer models of the Canfield joint are presented in Chapter 5.

[2]For the optical communication use case, the continuing efforts to validate the prototype described in Chapter 4 represent an increase from TRL 3 (Analytical and experimental critical function and/or characteristic proof-of-concept) to TRL 4 (Component and/or breadboard validation in laboratory environment).[7]

2 Background

2.1 Gimbals

Pointing is a necessary component of many engineering applications. The first pointing device developed, and the most commonly used, is the gimbal, an assembly of orthogonally mounted concentric rings. "Gimbaled" is commonly used as a transitive verb to denote orientation control in general, particularly with regard to thrusters. Passive gimbals appear since antiquity in domestic applications as a means of isolating mechanisms or containers of liquid from rotation, particularly on boats. An early description of a gimbal mechanism is credited to Philo of Byzantium, who described an inkpot gimbaled to remain upright without spilling. Gimbaled incense burners appear in China during the second and third century BCE. Roman historian Athenaeus Mechanicus describes[8] the use of gimbals to yoke siege machines to the decks of ships:

> *"When, you see, they plan to take a coastal city, certain master-builders are in the habit of yoking the machines onto merchant-ships in calm waters and taking them towards the walls; but if they are caught unawares by the wind and a wave is nurtured which swamps the vessels, the machine which has been attached rolls around, as the vessels are not making the same movement; hence, with the machines breaking up, boldness is induced in the enemy... One must therefore fix on the platform attached to the merchant-ships in the middle*

> *the [gimbal suspension], so that the machine stays upright in any inclination as the billow shakes it...”*

Active (i.e., driven) gimbals are commonly used in space and military applications. Several such gimbals are listed on page 12.

2.1.1 Gimbal Lock

Gimbal lock is a singular configuration in which the concentric rings of a gimbal are rotated such that two of the three axes are parallel, resulting in the loss of a degree of freedom. The gimbal does not get stuck in this position, but temporarily loses the capability to revolve around one axis. A common remedy is the addition of a redundant fourth ring, which adds complexity and mass, but simplifies control.

2.2 Parallel Robots

In a parallel manipulator, sometimes called a closed chain manipulator, two or more series chains connect the end effector to the base of the robot. The state of joints at the end effector can then be controlled by actuators at the base, resulting in a lighter robot overall, since the actuators at the base don’t have to support the weight of more actuators above them in addition to the weight of the links. The multiple chains also comprise multiple load paths, enabling the robot to support heavy loads. These advantages come at the cost of reduced workspace and more difficulty with obstacle avoidance than comparable serial (open-chain) linkages. Additionally, the nature of closed chains complicates the forward kinematics of parallel linkages. Still, parallel linkages have found a home in industrial robotics since its inception — a patent for a spray-painting robot, shown in Figure 2.1, was filed in 1942. Like the Canfield, it has three degrees of freedom and routes cables through a central chase, although the legs are asymmetric and the arrangement of joints is slightly different.[9] A range of 3 DoF parallel manipulators are in active usage in industrial applications. The most common and best-known is the delta robot, which has three kinematic chains of the RRPaR type.[10] Developed by Clavel in 1988, the delta is used in pick-and-place applications, for rapid transfer of light loads, and in additive manufacturing applications. Pollard's mechanism may be considered an ancestor of the delta. One variant of the delta, the Linapod, replaces its rotary actuator and lever with a linear actuator. Another familiar parallel linkage is the Stewart platform, attributed independently to Stewart, Gough, and Cavell. The Stewart platform is a 6 DoF parallel robot with prismatic joints, commonly used in flight simulators, where its parallel structure enables it to support significant weight. Further variants and other 3 DoF parallel manipulators are enumerated by Merlet.[10] Parallel architectures have also been developed for microelectrical/mechanical systems (MEMS). Several three-dimensional architectures similar to the Canfield are surveyed by Bamberger.[11] [1]

2.3 Canfield Joint

2.3.1 Structure

The Canfield joint consists of two triangular plates of equal size connected by three symmetric legs, where each leg has a universal joint (3 DoF) in the middle of its length and is connected to each plate by a revolute joint (1 DoF each). The top (distal) half of the Canfield joint is passive: movement is achieved by controlling the

[1]Notably, the means of realizing similar architectures in the context of MEMS manufacturing, where actuated revolute joints are a proven technology and 3D architectures are common, may offer lessons for additive manufacturing of Canfield joints.

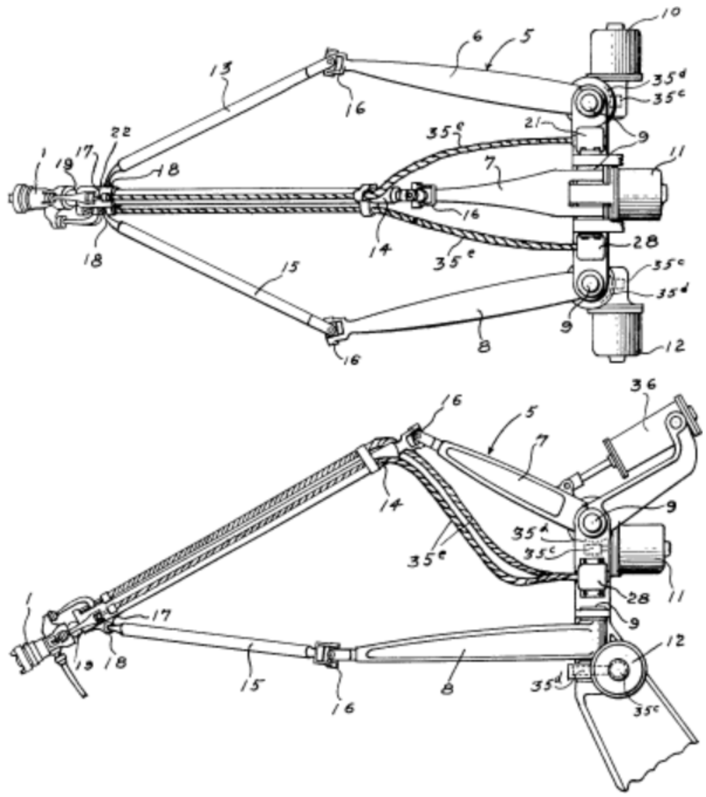

Figure 2.1. Among the first industrial robot designs, a parallel linkage intended for spray painting, similar to a delta robot. Designed by Willard Pollard in 1942.[2]

angles of the three basal legs. Notably, the midjoints of the joint are not driven. The kinematic chain, either 3-$\underline{\mathrm{R}}$UR or 3-$\underline{\mathrm{R}}$RRRR,[2] removes the need for linear actuators.

The patent[12] expired in 2001, so the joint is now in the public domain.

2.3.2 Advantages

The Canfield benefits from the advantages of parallel linkages listed above — (1) increased strength and (2) reduced weight compared to serial actuators. It is notable among parallel actuators for having a relatively large workspace and angular range[6], enabling its use for some applications traditionally reserved for serial linkages. The

[2]The specifics of the kinematic chain are discussed in Section 3.1.1.

use of revolute, rather than prismatic, driven joints is another advantage for reducing size, weight and power. The structure of the Canfield joint allows for its center to act as a cable chase; it was originally proposed under the name "carpal wrist joint," and its construction lends itself to prosthetic wrists, largely because the central cable runmimics a carpal tunnel. One of the key advantages of the Canfield joint is its capacity to "fail gracefully" when one leg freezes. Since load paths exist between each of the motors and the passive top halves of the opposing legs, a significant pointing workspace can still be achieved with only two degrees of freedom. The size of this workspace varies according to the angle of the frozen leg, but in most cases the joint can retain significant partial operation until repair is possible. In a deep space application, where the robot is remotely controlled but unrecoverable in the case of a failure, this capability allows its use to continue.

2.4 Pointing Applications

Previous NASA projects have explored the use of the Canfield joint for pointing solar cells and thrusters.

2.4.1 Solar Cell Tracking

The Canfield joint was researched for solar tracking applications at NASA Marshall Space Flight Center[13] in the Momentum-Exchange/Electrodynamic Reboost (MXER) project. Its hemispheric pointing workspace allows solar cells to remain pointed at the sun as the spacecraft rotates, and the power cables to the solar cells, routed through the center of the Canfield joint, will not tangle.[13]

2.4.2 Thrusters

The Canfield joint was also proposed as a mounting scheme for thrusters in the reaction system of the Crew Exploration Vehicle (CEV), a part of the now-defunct Constellation program which was later folded into Orion. Reaction control systems for spacecraft commonly use orthogonally mounted thruster quads like those highlighted in Figure 2.2 to provide attitude control. The engines in the quad may be fired in combination to generate a moment of force and thus reorient the spacecraft. In the system proposed, each thruster quad would be replaced by a single Canfield joint directing a single thruster, reducing weight and providing better fuel efficiency[14] because it would eliminate the canceled thrust components produced by firing two orthogonal thrusters. A prototype Canfield joint with a mounted thruster, controlled by joystick, was constructed[15] to demonstrate this functionality.

2.5 Integrated Radio and Optical Communication Project

The goal of iROC is to implement deep space optical communication from Mars to Earth, with proven radio communication protocols as a fallback. This is to be accomplished by a composite "teletenna" combining an RF reflector and Cassegrain geometry telescope for RF and optical communications, respectively. A similar combined design was proposed by Aviv.[16]

The pointing requirements for deep space optical communication are more onerous than for radiofrequency communication. In the case of iROC, the laser dot projected on the Earth is approximately the size of Texas. Per Table 2.1, an analysis found no

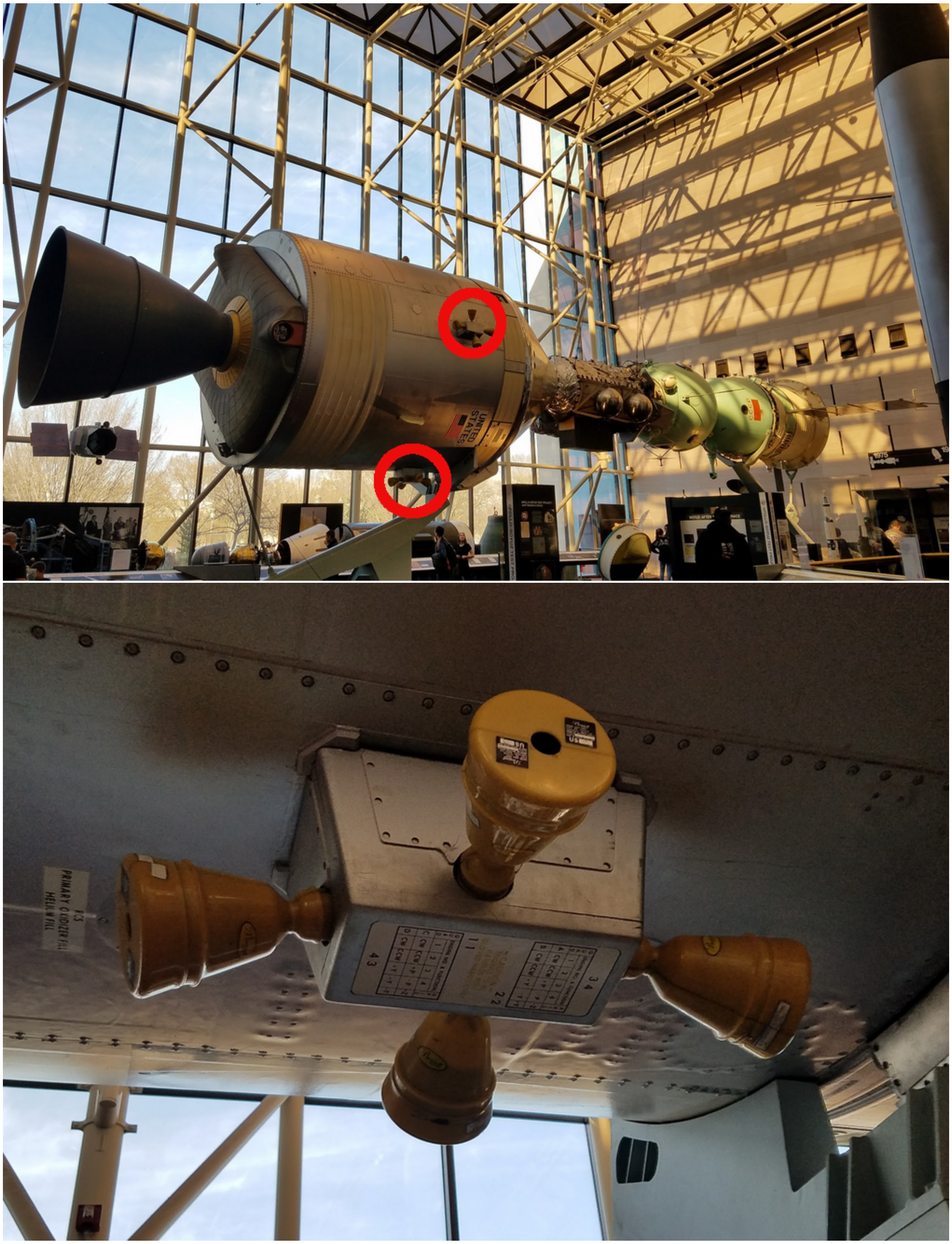

Figure 2.2. Model of the Apollo-Soyuz union in the National Air and Space Museum, with model of quad thruster highlighted. Thruster quads such as this one could be replaced with a Canfield joint for improved fuel efficiency.

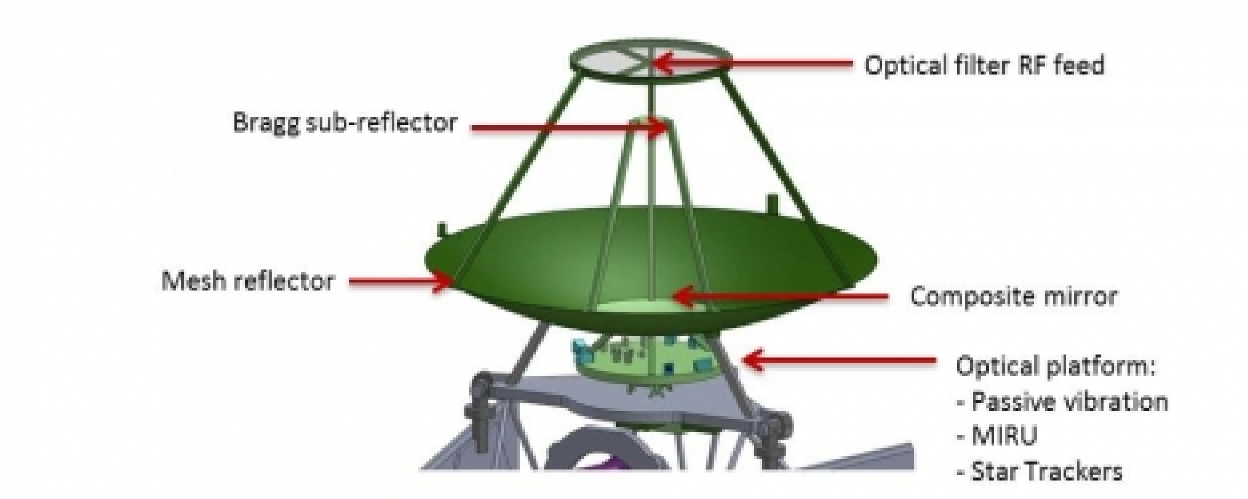

Figure 2.3. Schematic of iROC's potential 32 GHz RF/optical teletenna.

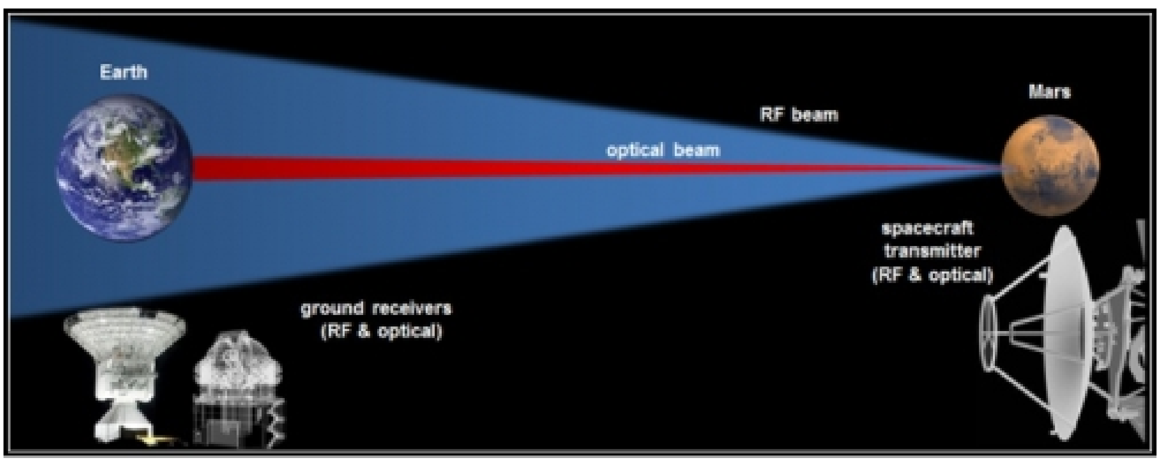

Figure 2.4. Illustration of proposed iROC architecture.

available COTS gimbals that satisfy the iROC requirements, particularly the articulated mass requirement. Further information on the project requirements is included in Chapter 4.

A prototype Canfield joint for the iROC project has been successfully fabricated and is currently under test, as shown in Figure 4.1.

Table 2.1. Review of available gimbals qualified for deep space operation from Moog™versus preliminary iROC pointing requirements.[1] AZ denotes azimuth, EL elevation, DS deep space, and LEO low earth orbit.

Parameter	**Units**	**Required for iROC**	**Moog Type 22**	**Moog Type 33 MUSES**	**Moog Type 33SHE**	**Moog Type 55**	**Moog EPGA**
Coverage	AZ deg	DS: 330	165	200	12.6	350	350
	EL deg	DS: 165	165	165	12.6	180	180
Pointing	deg	0.0115	0.01	0.01	0.01	0.006	0.002
Step Size	deg	0.057	0.02	0.009375	0.002	0.0075	0.002
Tracking rate	deg/s	DS:1 LEO: 0.02	0.02	0.1	0.02	0.0075	0.002
Slew rate	deg/s		9	3	3	2.25	0.6
Running torque	in-lbs N-m		150 18	300 34	300 34	500 56	950 100
Gimbal mass	kg	90	3.4 - 5	5.23	4.6	4.8	6.1
Power/axis	W		10	17	17	12	10
Volume	(in x in x in)		7.22 x 7.22 x 14.1	6.36 x 6.36 x 9.8	6.97 x 6.62 x 8.89	16.25 x 9.1 x 9.3	5.8 x 6.6 x 11.9
Controller	(kg)		1	1	1	1	1
Power	W @ V		1.5 @ 30	1.5 @ 30	1.5 @ 30	1.5 @ 30	1.5 @ 30

2.6 Kinematics of Parallel Manipulators

As with serial mechanisms, two kinematics problems must be solved for a parallel mechanism: The *forward kinematics,* which determines the position of the tool frame based on the positions of the driven joints, and the *inverse kinematics,* which provides the set of possible joint positions that lead to a given toolframe position. The set of all positions that can be reached with the end effector is the *workspace.*

2.6.1 Enumeration of of Kinematic Chains

The following system of enumeration for parallel manipulators developed by Tsai[17] is used in Chapter 3:

C: Cylindric joint

C_k: Connectivity of limb k hich is defined as the degrees of freedom associated with all the joints of limb k

F: degrees of freedom of a mechanism

P: prismatic joint

R: revolute joint

S: spherical joint

U: universal joint

m: number of limbs in a parallel manipulator

n: number of links in a mechanism

j: number of joints in a mechanism, assuming that all the joints are binary

f_i: degrees of freedom associated with joint i

L: number of independent loops in a mechanism

λ: freedom of the space in which a mechanism is intended to function

A kinematic chain is labeled according to its joints, with driven joints underlined. The kinematic chain of a single leg of the Canfield is $\underline{\text{R}}$UR, so the linkage is denoted 3-$\underline{\text{R}}$UR.[3]

2.6.2 Product of Exponentials Method

The product of exponentials (POE) method[18] is a robotics convention for mapping the links of a spatial kinematic chain. It uses two frames of reference — the base and tool frames — and, unlike Denavit-Hartenberg parameterization, does not require that the tool frames be particularly selected in order to achieve specific cancellations.

[3]See Section 3.1.1.

Define Zero Configuration. The first step is to select a "zero configuration" where all the joint angles are defined as being zero. The 4x4 matrix $g_{st}(0)$ describes the transformation from the base frame to the tool frame in this configuration. It is an affine transform consisting of the 3x3 rotation matrix R and the 1x3 translation vector p, augmented to create a 4x4 square matrix.

Define Origin and Axis of Action. For each joint of the kinematic chain, an origin point q and an axis of action are selected for the zero configuration, using the coordinate frame of the base. In the case of a prismatic joint, the axis of action v is the vector along which the joint extends; in the case of a revolute joint, the axis of action the vector normal to the rotation.

Find Twist for Each Joint. A 1x6 twist vector is composed to describe the movement of each joint. For a revolute joint,

$$\xi = \begin{pmatrix} -\omega \times q \\ \omega \end{pmatrix}$$

For a prismatic joint,

$$\xi = \begin{pmatrix} v_i \\ 0 \end{pmatrix}$$

The resulting twist has two 1x3 vector components: Linear motion along an axis (v) and rotational motion along the same axis (ω).

$$\xi = \begin{pmatrix} v \\ \omega \end{pmatrix}$$

Calculate Rotation Matrix. The 1x3 vector ω is rewritten in cross product matrix notation as the skew-symmetric matrix

$$\hat{\omega} = \begin{bmatrix} 0 & -\omega_3 & \omega_2 \\ \omega_3 & 0 & -\omega_1 \\ -\omega_2 & \omega_1 & 0 \end{bmatrix}. \tag{2.1}$$

.

Per Rodrigues' rotation formula, the rotation matrix is calculated from the rotational component:

$$e^{\hat{\omega}\theta} = I + \hat{\omega}\sin\theta + \hat{\omega}^2(1 - \cos\theta), \tag{2.2}$$

Calculate Translation Vector. The 1x3 translation vector p_i is calculated from the components of the twist.

$$(I - e^{\hat{\omega}\theta})(\omega \times v + \omega\omega^T v\theta) \tag{2.3}$$

Compose Matrix Exponential. For each joint i, the matrix exponential $e^{\hat{\xi}_{ij}\theta_{ij}}$ for a given joint angle θ is calculated according to the formula:

$$e^{\hat{\xi}_{ij}\theta_{ij}} = \begin{bmatrix} e^{\hat{\omega}\theta} & p_i \\ 0 & 1 \end{bmatrix}, \tag{2.4}$$

where I is the 3x3 identity matrix.

Compose Structure Equation. The matrix exponentials are multiplied to produce a 4x4 affine transform $g_d(\theta_1...\theta_N)$ from the base frame to the tool frame of a manipulator with N joints in a given configuration defined by joint positions $\theta_1...\theta_N$.

$$g_{st} = e^{\hat{\xi}_1\theta_1}...e^{\hat{\xi}_N\theta_N} g_{st}(0) \tag{2.5}$$

Structure Equation for Parallel Manipulators. In a parallel manipulator, the structure equations for each of the legs are equal. For a parallel manipulator with three legs, such as the Canfield:

$$g_{st} = e^{\hat{\xi}_{11}\theta_{11}} ... e^{\hat{\xi}_{1n_1}\theta_{1n_1}} g_{st}(0) = e^{\hat{\xi}_{21}\theta_{21}} ... e^{\hat{\xi}_{2n_2}\theta_{2n_2}} g_{st}(0) = e^{\hat{\xi}_{31}\theta_{31}} ... e^{\hat{\xi}_{3n_3}\theta_{3n_3}} g_{st}(0). \quad (2.6)$$

2.7 Summary

The Canfield joint offers advantages for a range of applications in space and industry. Performing a rigorous engineering analysis for optical communication, the application most constrained by pointing requirements, will open up its use for other applications as well.

3 Kinematic Analysis

The Canfield joint is counterintuitive to control because the angular positions of the base angles do not map directly to the orientation of the distal plate. Canfield's original work presents solutions for the forward and inverse kinematics of the linkage, as well as an analysis of the singularities[6]. Herein, an overview of the original work and alternative derivations are presented to simplify position control for future engineering applications.

This chapter presents two approaches to kinematic analysis of the Canfield joint. The first is a geometric analysis based on Canfield's original work, as well as work undertaken in collaboration at NASA Glenn with Robert Short[19] and Christian Bueno[20]. This is followed by an analysis using the product of exponentials method[18].

3.1 Model

The Canfield joint's geometry may be best understood in terms of the **midplane** formed by the midjoints of the three legs, as shown in Figure 3.1. Only the joint angles surrounding the **base plate** are driven, and the configuration of the entire structure may be inferred from their states. The position of the **distal plate** (shown in Figure 3.3) can be found by reflecting the base plate across the midplane. The

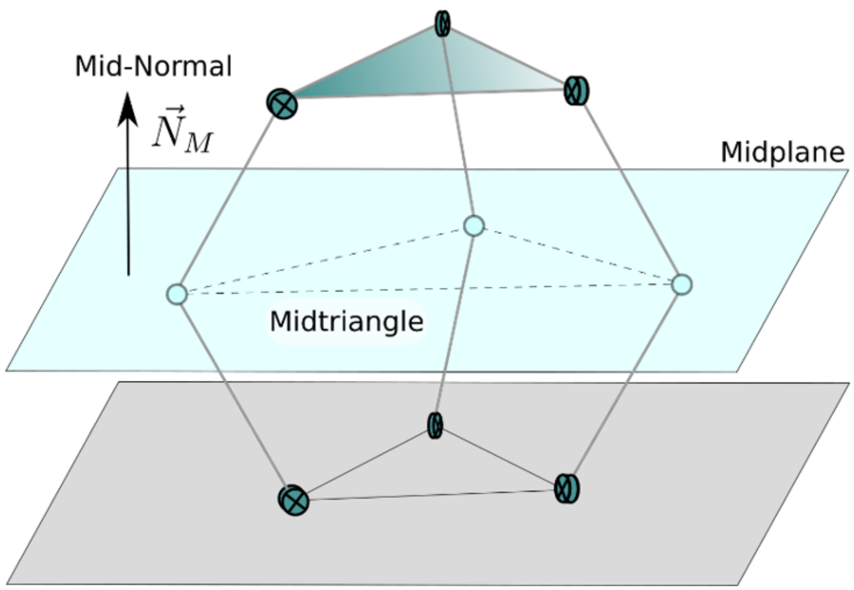

Figure 3.1. Illustration of the midplane. The distal plate is at the top; the base, at the bottom. Image credit: Christian Bueno.

geometric analysis uses a simplified model of the legs, where the three revolute joints are considered as a single spherical joint.

3.1.1 A Note on Midjoint Variations

Original sources[6] and the geometric model used in this section rely on the assumption that the legs of the Canfield joint are in-line; that is, that the base and distal plates, when the joint is collapsed, are congruent. This is achieved in Canfield's prototype by means of a universal joint, which is singularity-free; its kinematic chain may be written as 3-$\underline{\text{R}}$UR. However, the prototype tested in Chapter 4 and the model shown in Section 5.1.2 replace the central universal joint with three successive revolute joints, resulting in a kinematic chain of 3-$\underline{\text{R}}$RRRR, where the width of the central joint must be considered as an additional link. As shown in Figure 3.2, the iROC prototype's

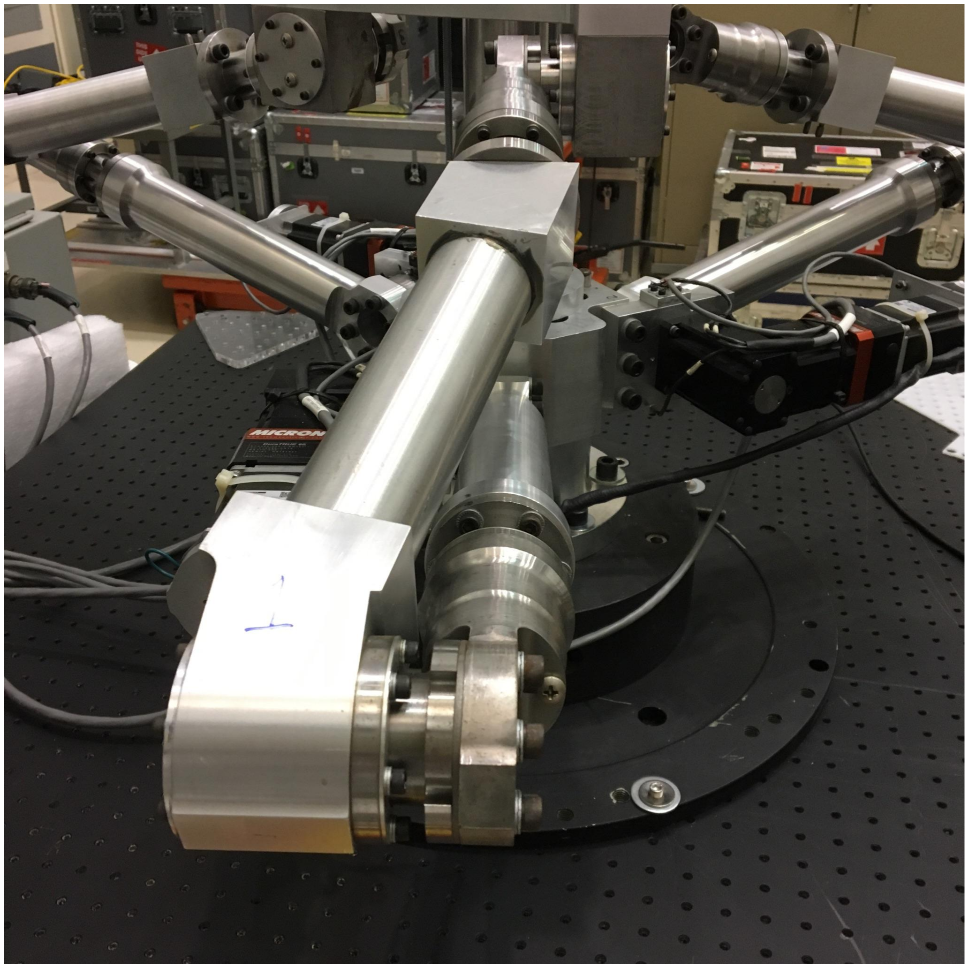

Figure 3.2. Leg of Canfield prototype.

legs are angled to preserve the congruence of the plates. The differences in the 3-$\underline{R}$RRRR version may complicate the manipulator kinematics to a degree which, for the high-precision requirements of this application, should be addressed in future work. Possible impacts of this design are addressed in Section 3.4.

3.1.2 Reference Frame

The reference frame for the joint is defined such that the origin lies at the center of the base plate with the z-axis normal to the base plate and the x-axis aligned along the first leg, as in Figure 3.4. Looking along the z-axis in the negative direction, the

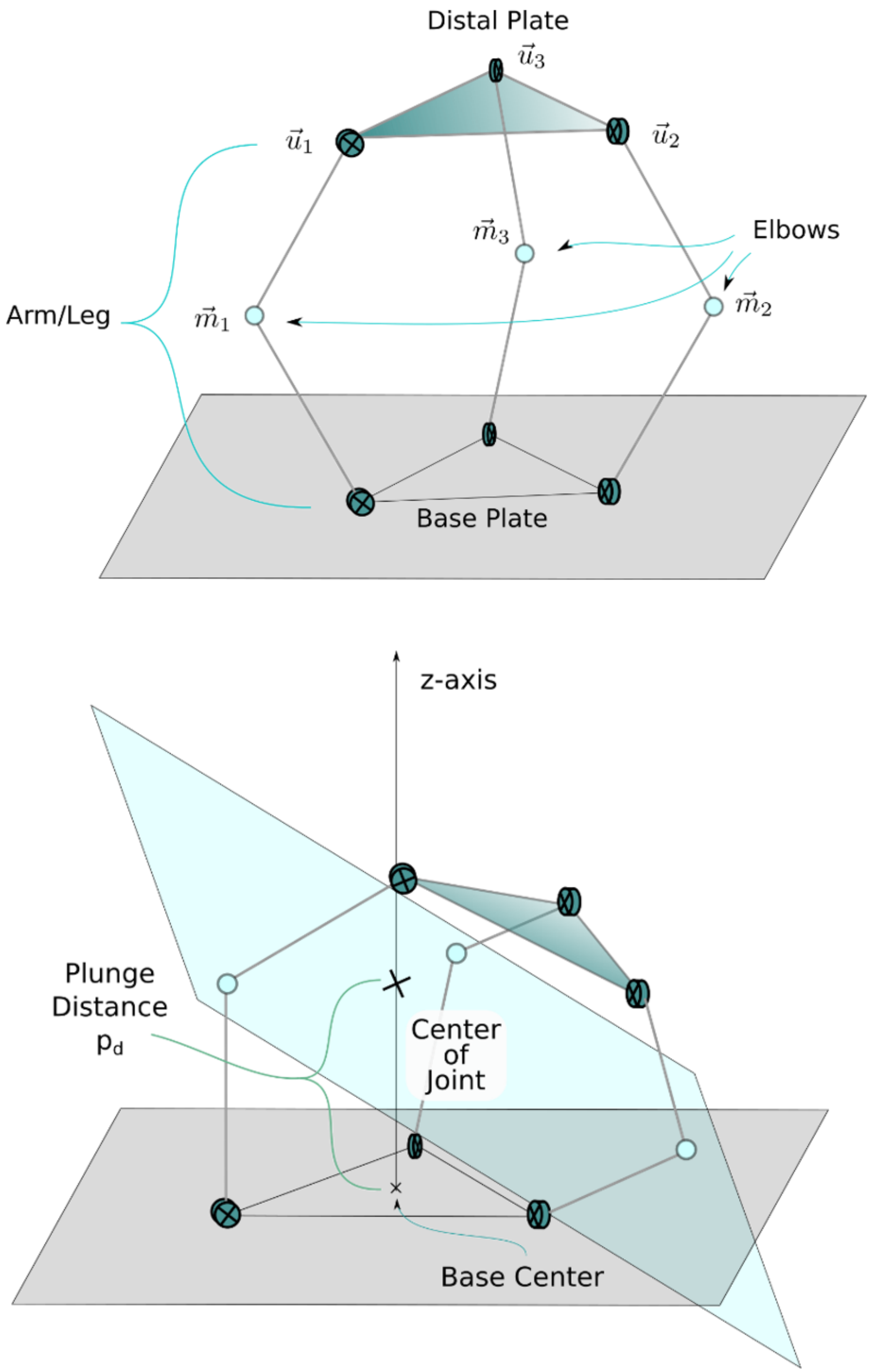

Figure 3.3. Illustration of the parts of the Canfield joint. Image credit: Christian Bueno.

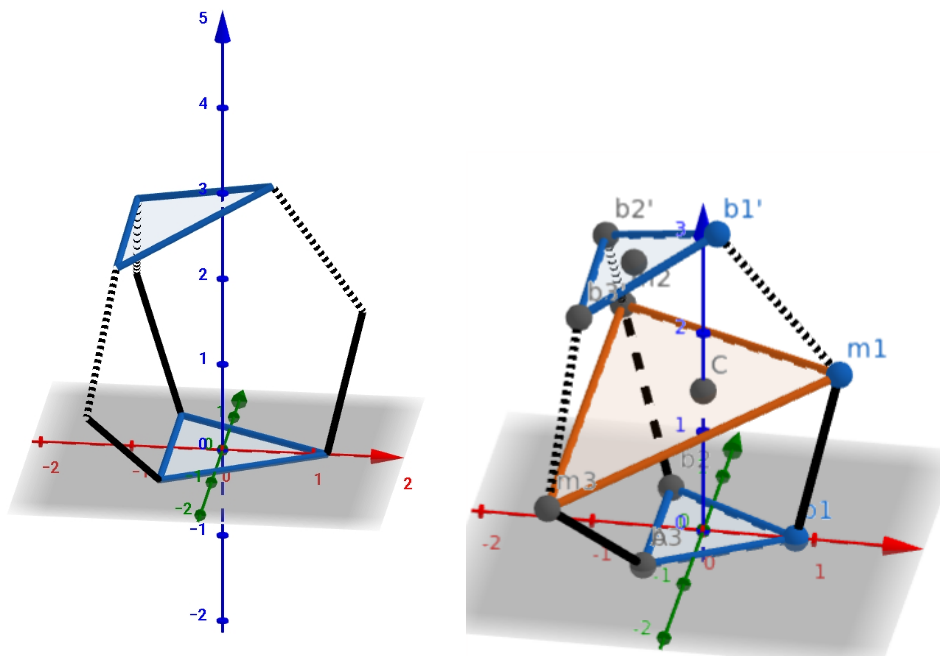

Figure 3.4. Simplified model of the Canfield with coordinate frame, approximating the revolute leg joints as a single spherical joint. On the right, points are labeled and the midtriangle is highlighted.

legs are numbered counterclockwise, so that the vectors defining the direction of each leg are:

$$\boldsymbol{b}_1 = \left\langle \frac{b}{\sqrt{3}}, 0, 0 \right\rangle, \tag{3.1}$$

$$\boldsymbol{b}_2 = \left\langle -\frac{b}{2\sqrt{3}}, \frac{b}{2}, 0 \right\rangle, \text{ and} \tag{3.2}$$

$$\boldsymbol{b}_3 = \left\langle -\frac{b}{2\sqrt{3}}, -\frac{b}{2}, 0 \right\rangle, \tag{3.3}$$

per standard right-hand convention.

3.2 Geometric Analysis

The following variables are used in the geometric analysis:

θ_i**:** Base angle of leg i

$\mathbf{N}_m$**:** Midplane normal vector

$\mathbf{m}_i$**:** Vector from base to midjoint of leg i

$\mathbf{c}_i$**:** Cosine of θ_i

$\mathbf{s}_i$**:** Sine of θ_i

$\mathbf{p}_d$**:** Plunge distance

D: Distal plate origin

C: Center of Canfield joint

l: Leg length

b: Base length

3.2.1 Midplane Construction

The $\boldsymbol{m}_i$ vectors, which define the positions of the three midjoints relative to the origin at the center of the base plate, may be constructed by first rotating a length ℓ vector around the correct hinge and then translating this to the correct hinge location. Let $c_i = \cos(\theta_i)$ and $s_i = \sin(\theta_i)$. Then,

$$\boldsymbol{m}_1 = \ell \left\langle c_1, 0, s_1 \right\rangle + \boldsymbol{b}_1, \tag{3.4}$$

$$\boldsymbol{m}_2 = \ell \left\langle -\frac{c_2}{2}, \frac{c_2\sqrt{3}}{2}, s_2 \right\rangle + \boldsymbol{b}_2, \text{ and} \tag{3.5}$$

$$\boldsymbol{m}_3 = \ell \left\langle -\frac{c_3}{2}, -\frac{c_3\sqrt{3}}{2}, s_3 \right\rangle + \boldsymbol{b}_3. \tag{3.6}$$

$\boldsymbol{N}_m$, the normal vector to the midplane, is by definition:

$$\boldsymbol{N}_m = (\boldsymbol{m}_2 - \boldsymbol{m}_1) \times (\boldsymbol{m}_3 - \boldsymbol{m}_1), \text{ or} \tag{3.7}$$

$$\boldsymbol{N}_m = \boldsymbol{m}_1 \times \boldsymbol{m}_2 + \boldsymbol{m}_2 \times \boldsymbol{m}_3 + \boldsymbol{m}_3 \times \boldsymbol{m}_1. \tag{3.8}$$

3.2.2 Plunge Distance

The center of the joint is defined as the point at which a vector normal to the base plate intersects the midplane. For a plunge distance p_d, the center is $\langle 0, 0, p_d \rangle$. In this frame of reference, the line is parametrized by $\langle 0, 0, t \rangle$, for $t \in \mathbb{R}$, and the plane is computed as $\boldsymbol{N}_m \cdot \langle x, y, z \rangle = \boldsymbol{N}_m \cdot \boldsymbol{m}_1$. Thus, $\boldsymbol{N}_m \cdot \langle 0, 0, t \rangle = \boldsymbol{N}_m \cdot \boldsymbol{m}_1$. Given the formula for $\boldsymbol{N}_m$ in Equation 3.7 in conjunction with the fact that $t = p_d$ for the intersection (by definition of the center and the selected parameterization of the line), $p_d(\boldsymbol{N}_m \cdot \hat{\mathbf{k}}) = \boldsymbol{m}_1 \cdot (\boldsymbol{m}_1 \times \boldsymbol{m}_2 + \boldsymbol{m}_2 \times \boldsymbol{m}_3 + \boldsymbol{m}_3 \times \boldsymbol{m}_1) = \boldsymbol{m}_1 \cdot (\boldsymbol{m}_2 \times \boldsymbol{m}_3)$. This yields the following formula for the plunge distance:

$$p_d = \frac{\boldsymbol{m}_1 \cdot (\boldsymbol{m}_2 \times \boldsymbol{m}_3)}{\boldsymbol{N}_m \cdot \hat{\mathbf{k}}}. \tag{3.9}$$

3.2.3 Distal Normal Vector

A formula may now be determined for the normal vector to the distal plate. Notice that the normal vector to the base plate (the z-axis) intersects the midplane at $\boldsymbol{C} = \langle 0, 0, p_d \rangle$. We can locate the center of the distal plate by reflecting the vector $-\boldsymbol{C}$ over the midplane. The formula for reflecting a vector over a plane through the origin with normal vector $\boldsymbol{N}$ is given by $\boldsymbol{r}_{\boldsymbol{N}}(\boldsymbol{v}) = \boldsymbol{v} - 2\frac{\boldsymbol{v} \cdot \boldsymbol{N}}{||\boldsymbol{N}||^2}\boldsymbol{N}$. For our purposes, we can first reflect $-\boldsymbol{C}$ over the plane through the origin with normal vector $\boldsymbol{N}_m$, then we translate up by $\boldsymbol{C}$ in order to locate the center of the distal plate $\boldsymbol{D}$. That is,

$\boldsymbol{D} = \boldsymbol{r}_{\boldsymbol{N}_m}(-\boldsymbol{C}) + \boldsymbol{C}$. Substituting the values into the formula and solving yields the following:

$$\boldsymbol{D} = 2\left(\frac{p_d(\boldsymbol{N}_m \cdot \hat{\mathbf{k}})}{||\boldsymbol{N}_m||^2}\right)\boldsymbol{N}_m = 2\left(\frac{\boldsymbol{m}_1 \cdot (\boldsymbol{m}_2 \times \boldsymbol{m}_3)}{||\boldsymbol{N}_m||^2}\right)\boldsymbol{N}_m \tag{3.10}$$

where $\hat{\mathbf{k}}$ is the unit z axis for the base coordinate frame.

The normal vector to the distal plate is then given by $\boldsymbol{D} - \boldsymbol{C}$. In other words, the normal vector to the distal plate is $\boldsymbol{r}_{\boldsymbol{N}_m}(-\boldsymbol{C})$, the reflection vector given in the formula.

3.2.4 Distal Frame (Forward Kinematics)

The 4x4 matrix encoding the transform from the base origin to the distal plate may be expressed in terms of the functions described above. First, the position vector p is drawn directly from the value of D above. Next, the 3x3 rotation matrix R is obtained by reflecting the origin's coordinate frame (the 3x3 identity matrix) over the midplane.

The reflection of a vector v, where $\bar{p_d} = (0, 0, p_d)^T$:

$$R_M(v) = v - 2\frac{(v - p_d)\dot{N}_m}{N_m\dot{N}_m}N_m$$

This yields the 4x4 matrix

$$g_{st}(\theta) = \begin{bmatrix} R & p \\ 0 & 1 \end{bmatrix} \tag{3.11}$$

where the rotation component is caluclated by applying the rotation above to the 3x3 identity matrix:

$$R = R_M(I^3),$$

and the translation is drawn from the distal normal vector in Equation 3.10:

$$p = [D_x, D_y, D_z]^T.$$

in terms of the joint angles.

3.2.5 Az/El Coordinates

The azimuth and elevation, relative to the base frame, are calculated from $\boldsymbol{D}$. Azimuth is calculated from the X and Y components of $\boldsymbol{D}$:

$$AZ = \text{atan2}(D_y, D_x). \tag{3.12}$$

Elevation is the angle between the distal vector and the XY plane, which can be calculated from the dot product of the distal vector and the Z axis:

$$EL = \pi/4 - \frac{D \cdot Z}{|D||Z|}. \tag{3.13}$$

3.3 Product of Exponentials Method

The following section outlines the calculation of the kinematic chain of the joint per the product of exponentials (POE) method.[18] The variables in this analysis follow the method outlined in Section 2.6.2. In the POE analysis, θ_{ij} denotes the angle of joint j in leg i.

First, the zero-configuration transform from the base frame to the distal frame is found by inspection. The zero configuration is taken to be the legs extended straight up. No rotation is applied between the base and distal frames, so the rotation matrix

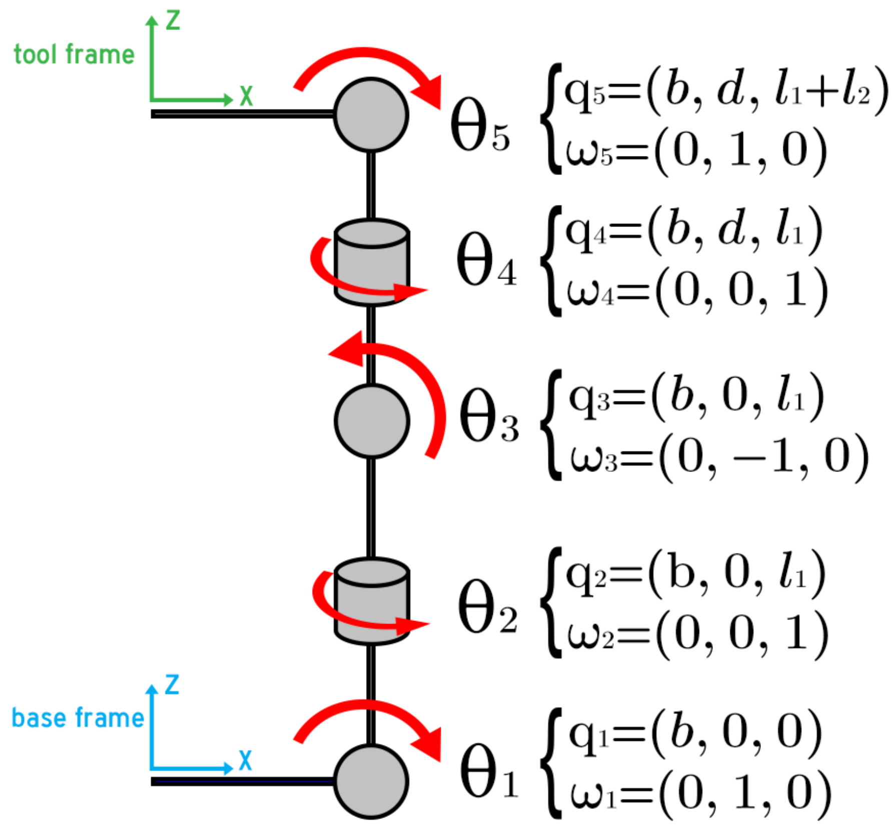

Figure 3.5. Kinematic chain of a single leg. The points denoted are specific to the leg oriented along the x-axis.

is merely a 3x3 identity matrix. The only translation component is the total length of the legs along the z-axis. Thus:

$$g_{st}(0) = \begin{bmatrix} R & p \\ 0 & 1 \end{bmatrix} = \begin{bmatrix} 1 & 0 & 0 & 0 \\ 0 & 1 & 0 & 0 \\ 0 & 0 & 1 & 2l \\ 0 & 0 & 0 & 1 \end{bmatrix} \tag{3.14}$$

Next, the kinematic chain for each leg must be calculated. The screws for each joint can be expressed in terms of the base hinges found in Equation 3.4 and the

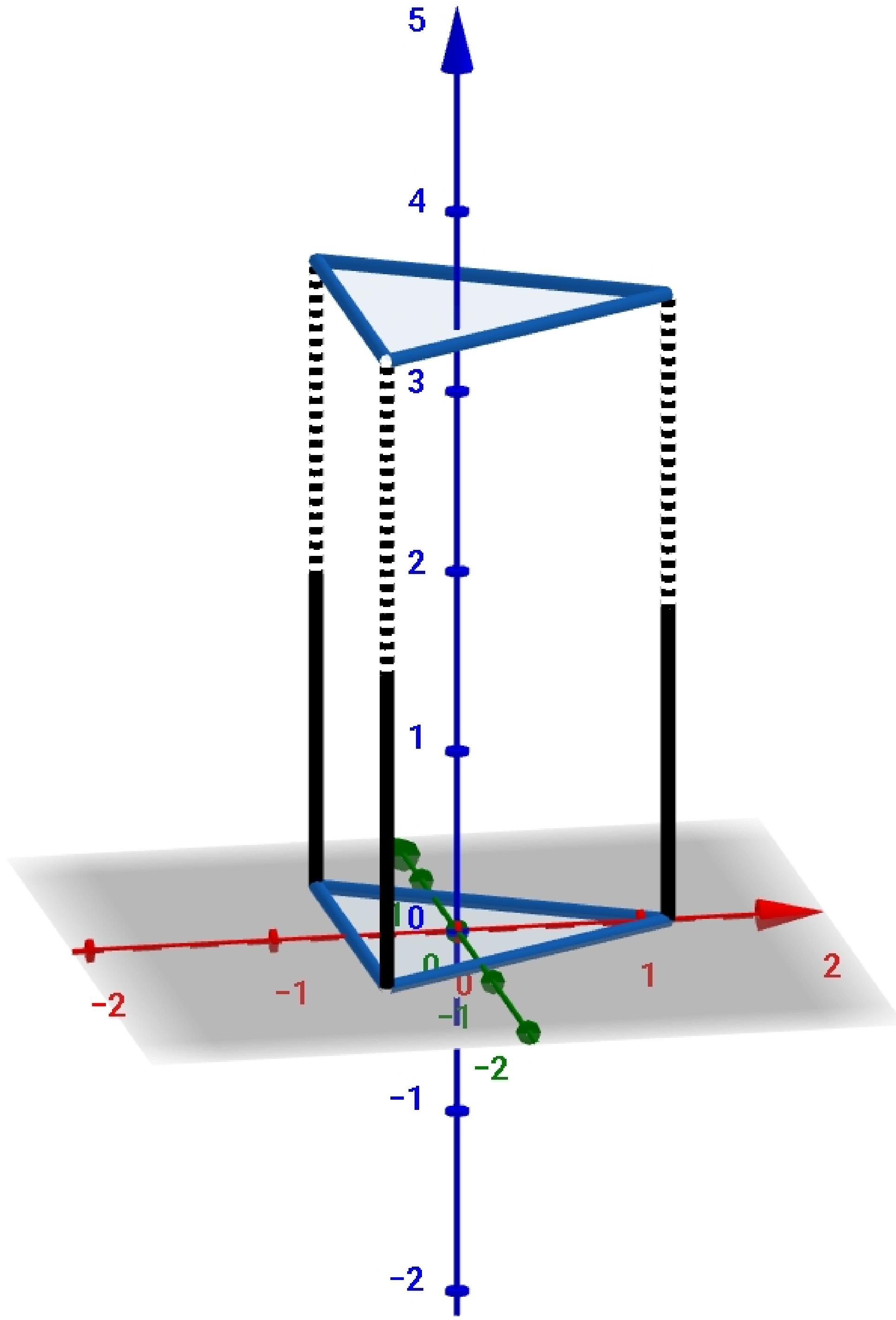

Figure 3.6. Zero configuration.

leg length l. The configuration of each leg is expressed in terms of 5 revolute joints, where the screw ξ_{ij} is calculated from the joint origin q_{ij} and the axis of action ω_{ij}.

For a revolute joint:

$$\xi = \begin{pmatrix} -\omega \times q \\ \omega \end{pmatrix} = \begin{pmatrix} v \\ \omega \end{pmatrix}.$$

Notably, the parameterization of the joint angles in this method is different from that in the geometric method, so that the zero configuration (Figure 3.5) used in the product of exponentials method is physically realizable. Where the parameterization shifts, the required shift from the respective geometric joint angle θ to the product of exponentials joint angle θ' is summarized in the table.

Table 3.1. Table of twists for the first kinematic chain, accounting for revolute joint width d.

Joint	q_N^T **(Origin)**	ω_N^T **(Vector)**	ξ_N^T **(Twist)**	θ **Difference**
1	[b, 0, 0]	[0, 1, 0]	$[0\ 0\ b\ 0\ 1\ 0]$	$\theta'_1 = \theta_1 - \pi/2$
2	[b, 0, l_1]	[0, 0, 1]	$[0\ -b\ 0\ 0\ 0\ 1]$	
3	[b, 0, l_1]	[0, -1, 0]	$[-l_1\ 0\ b\ 0\ 1\ 0]$	$\theta'_3 = \theta_3$
4	[b, d, l_1]	[0, 0, 1]	$[d - b\ 0\ 0\ 0\ 1]$	
5	[b, d, $l_1 + l_2$]	[0, 1, 0]	$[(l_1 + l_2)\ 0\ b\ 0\ 1\ 0]$	$\theta'_5 = \theta_5 - \pi/2$

For each screw, the matrix exponential $e^{\hat{\xi}_{ij}\theta_{ij}}$ for a given joint angle θ is calculated per the procedure outlined in Section 2.6.2.

From Table 3.1, the twists for Leg 1 are obtained based on two assumptions about the dimensions of the joint: First, that the leg lengths are equal ($l_1 = l_2 = l$); second, that the width d of the midjoint is zero, per the discussion in Section 3.1.1.

The twists for the other two kinematic chains are found by rotating ω and q around the z axis with the following rigid body transform:

$$R_z(\alpha) = \begin{bmatrix} \cos(\alpha) & -\sin(\alpha) & 0 \\ \sin(\alpha) & \cos(\alpha) & 0 \\ 0 & 0 & 1 \end{bmatrix}.$$

The value of α is $\pi/3$ for the second leg, and $2\pi/3$ for the third.

3.3.1 Forward Kinematics

The forward kinematics for a single leg may be found directly from the structure equation, which is the product of the matrix exponentials for each of the joints.

$$g_{st} = e^{\hat{\xi}_{11}\theta_{11}}...e^{\hat{\xi}_{1n_1}\theta_{1n_1}}g_{st}(0) = e^{\hat{\xi}_{21}\theta_{21}}...e^{\hat{\xi}_{2n_2}\theta_{2n_2}}g_{st}(0) = e^{\hat{\xi}_{31}\theta_{31}}...e^{\hat{\xi}_{3n_3}\theta_{3n_3}}g_{st}(0). \quad (3.15)$$

3.3.2 Inverse Kinematics: Paden-Kahan Subproblems

The inverse kinematics for the Canfield joint are complicated by the fact that the desired output - distal plate orientation - requires only two degrees of freedom, while the mechanism itself has three. The inverse kinematics may be solved by considering the inverse problem for each open-chain mechanism, i.e., each leg. These are solved with the Paden-Kahan subproblem method.[18]

Structure Equation. The subproblem begins with the structure equation of a single leg. To simplify notation, the matrix exponential $e^{\hat{\xi}_i\theta_i}$ will be written as e_i. For a desired transform g_d, the joint angles $\theta_1...\theta_6$ may be obtained through this method. The structure equation for a single leg is written:

$$g_d = e_1e_2e_3e_4e_5g_{st}(0). \quad (3.16)$$

The zero configuration transform $g_{st}(0)$ is known, so the twists are isolated on one side of the equation:

$$e_1e_2e_3e_4e_5 = g_d g_{st}^{-1}(0) =: g_1. \tag{3.17}$$

For a given twist ξ_i, the product of the matrix exponential e_i and a point p on the axis of the twist is equal to p. This allows for the selective elimination of some twists from the structure equation in order to solve for others.

Solve for θ_3. Both sides of Equation 3.17 are applied to the point $p_1 = [b, 0, l_1 + l_2]$, which is at the intersection of the fourth and fifth axes. This allows the latter two twists to be eliminated from the equation.

$$g_1p_1 = e_1e_2e_3e_4e_5p_1 = e_1e_2e_3p_1. \tag{3.18}$$

The point $p_2 = [b, 0, 0]$, which lies at the intersection of the first two axes, is subtracted from Equation 3.18:

$$g_1(p_1 - p_2) = e_1e_2(e_3(p_1 - p_2)) = e_3(p_1 - p_2). \tag{3.19}$$

Taking the magnitude of both sides of Equation 3.19:

$$||g_1(p_1 - p_2)|| = ||e_3(p_1 - p_2)||. \tag{3.20}$$

This puts the equation in the proper format to solve for θ_3 using Subproblem 5.

Solve for θ_1, θ_2. With the value of e_3 known, the point p_3 defined as e_3p_1. From Equation 3.18:

$$e_1e_2p_3 = g_1p_1. \tag{3.21}$$

This equation is in the correct form to solve for θ_1 and θ_2 using Subproblem 2.

Solve for θ_4, θ_5. Now that e_1, e_2 and e_3 are known, the remaining matrices may be isolated.

$$e_4 e_5 = e_3^{-1} e_2^{-1} e_1^{-1} g_1 =: g_2. \tag{3.22}$$

This equation may be applied to any point p_4 not on axes 4 and 5; $p_4 = [0, 0, 0]$ should suffice:

$$e_4 e_5 p_4 = g_2 p_4. \tag{3.23}$$

θ_4 and θ_5 may now be solved using Subproblem 2.

Number of Solutions. Subproblem 2 returns zero, one, or two possible pairs of real solutions, and Subproblem 5 returns one real solution. The procedure outlined here, therefore, may return up to four possible solutions for the inverse kinematics of a single leg at a given configuration. A correct solution for the inverse kinematics of the entire parallel linkage requires that the solutions for all three legs be congruent.

3.4 Singularity Analysis

A singularity is a configuration in which a robot loses a degree of freedom, and *instantaneous* movement in a certain direction is not possible. For example, in the case of an outstretched arm, where two rotational axes become collinear, the capacity to rotate around one axis is lost. Gimbal lock is another example of a singular configuration. Generally, these configurations are acceptable in trajectory planning: they may even be advantageous, as when an outstretched leg provides a strong load path. The robot can often move out of the singular configuration and regain the degree of freedom lost. However, the Canfield appears to be a kinematotropic linkage[21], i.e., a linkage for which a variation of position parameters can change its mobility. An example of this is shown in Figure 3.8: if the three midjoints become collinear and the joint topples as shown, it can no longer be controlled by the driven joints. It becomes, in a word, stuck. When the three midjoints becomes colocated, as in Figure 3.7, the Canfield loses its three original degrees of freedom, but gains two new ones that cannot be controlled. This behavior is indicative of a kinematotropic linkage. This configuration (which has been obtained on the prototype in Chapter 4) and others like it are obviously very undesirable, since they can destroy the robot's functionality. Therefore, these singularities should be identified and avoided[1] by the robot's control system.

3.4.1 Midplane Inspection

Since the position of the distal plate is defined by that of the midplane relative to the base, as discussed in Section 3.1, it follows that, if the midplane is underdefined (that is, if the midjoints are collinear or colocated, reducing the area of the midtriangle to zero), the number of possible solutions for the position of the distal plate becomes infinite, resulting in a singular configuration. Two singular configurations of this type are discoverable by inspection.[2] The first is the collinear configuration, where one of the legs bends inward so that the three midjoints become collinear, reducing the midplane to a line. The second is the "tipi" configuration, shown in Figure 3.7, where the three midjoints meet under the distal plate. In the first case, the range of

[1]Topologically, a kinematotropic singularity represents a "wormhole" to another configuration space. In engineering application, it is sufficient to consider it as something the robot should not be allowed to do.

[2]Readers are advised to make use of the 3D models discussed in Section 5.1.

possible locations for the distal center describes an arc around the line; in the second, it describes a hemisphere around the center point.

3.4.2 Single Chain Singularities

Two singular configurations affecting the Canfield joint are discoverable by examining the kinematic chain of a single leg. In both cases shown here (Figures 3.9 and 3.10), the axes ω_2 and ω_4 are aligned parallel to one another and orthogonal to axis ω_3, and rotation about the axis coming out of the page is impeded. These singularities may be specific to the 3-$\underline{\text{R}}$RRRR kinematic chain, as dicussed in Section 3.1.1.

Starfish Singularity. In the starfish singularity, shown in Figure 3.9, the joint collapses so that the base and distal plates are approximately congruent. The driven joints can move the midjoints up and down, but no torque is exerted on the distal plate. This singularity is discernible for individual legs, as well. Canfield's original prototype[22] has a mechanical stop to keep the midjoint from reaching this position. This is a known issue on the iROC prototype.

Leg Lock Singularity. The leg lock singularity, shown in Figure 3.4.2, is specific to the all-revolute kinematic chain. It occurs only when the distal plate is at its maximum distance from the base plate. If the midjoint of a leg is rotated to be orthogonal to the base and distal joints as shown, the leg cannot collapse. If the midjoint is compliant, slight torque in one direction or another can cause it to rotate and pull it out of the singular configuration. It's unknown whether this is an issue on the iROC prototype.

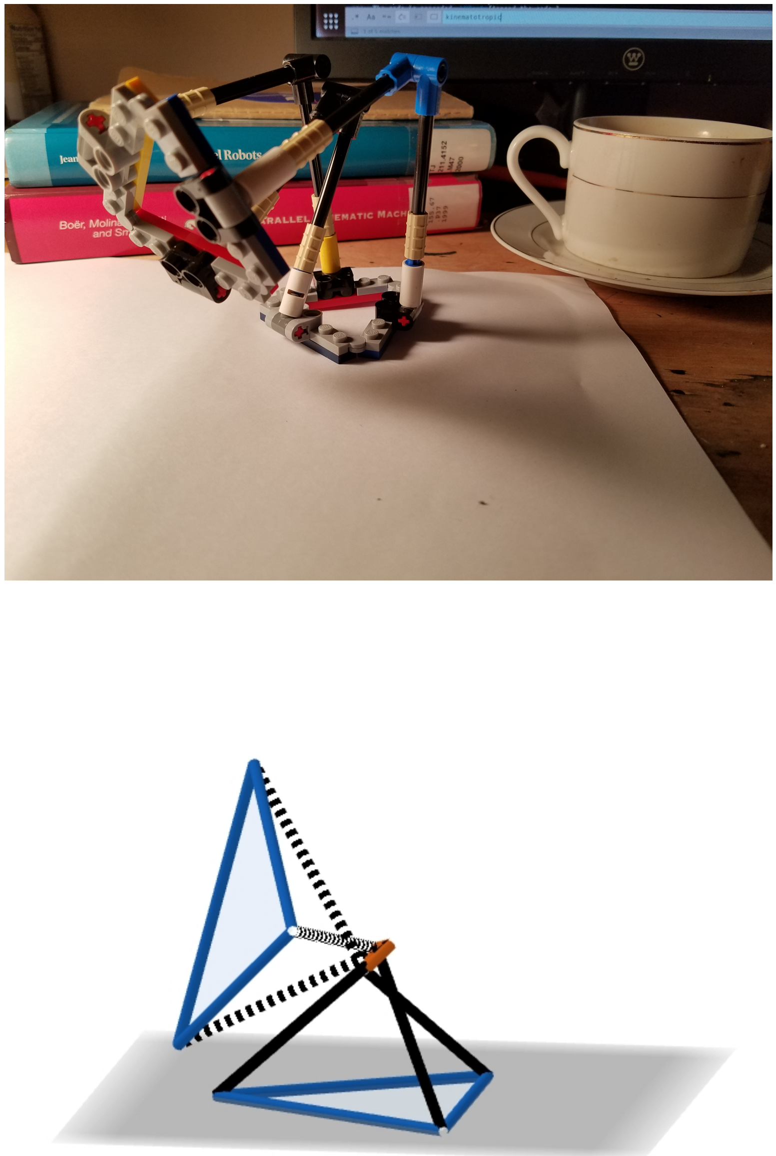

Figure 3.7. The "tipi" configuration. The midtriangle is reduced to a point. The range of possible solutions for the position of the distal plate forms a sphere around the point where the midjoints meet.

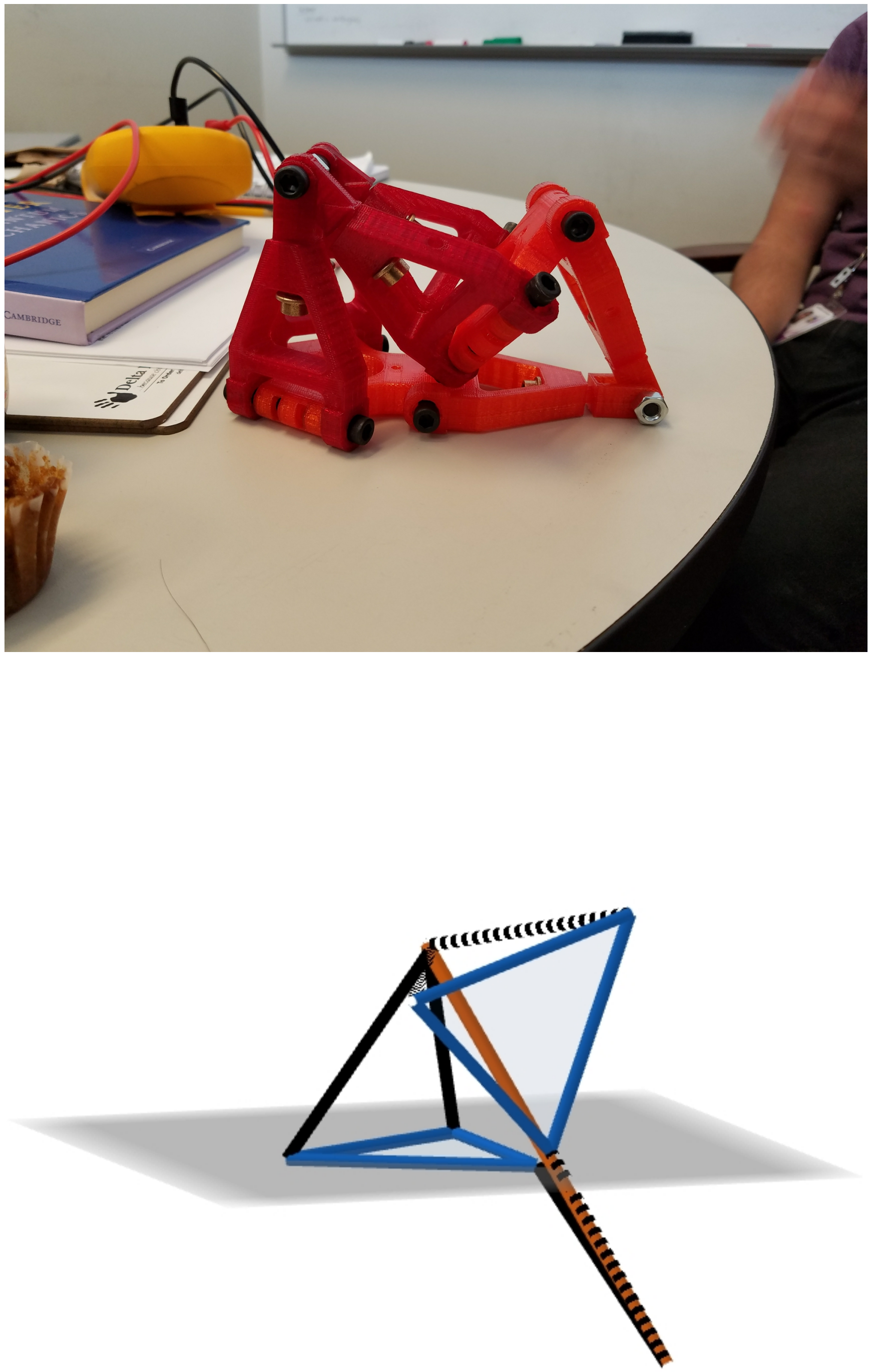

Figure 3.8. A collinear configuration, known colloquially as Alan's Singularity. In the virtual model, the midtriangle is reduced to a line.

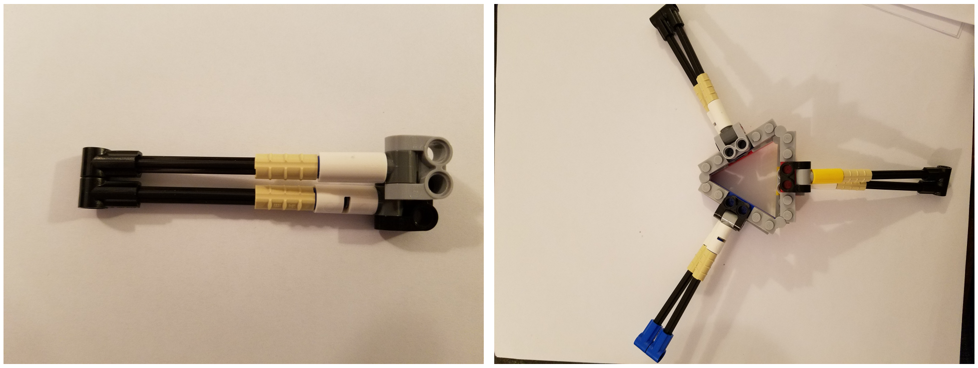

Figure 3.9. The “Starfish” singularity.

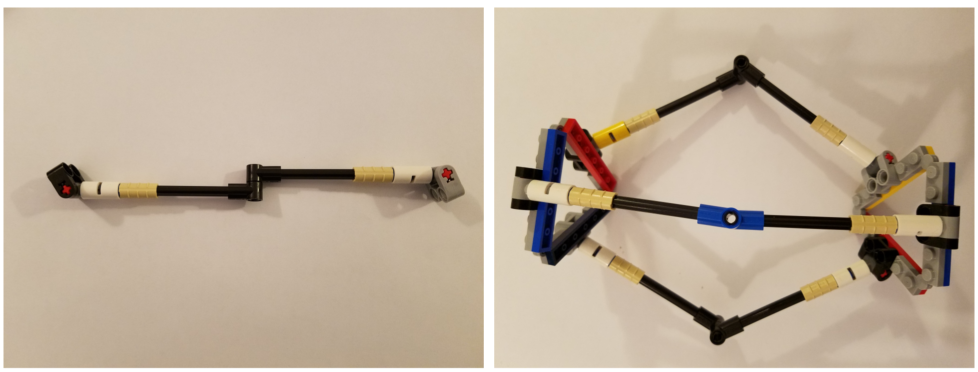

Figure 3.10. The leg-lock singularity.

3.5 Control Methods

Robotic position control may be achieved through two general methods: joint space and configuration space.

3.5.1 Joint Space Control

In joint space control, the positions for each degree of freedom are calculated based on kinematic equations. This can be achieved with the forward and inverse kinematics methods from the geometric and product of exponentials methods presented above.

3.5.2 Configuration Space Navigation

In the configuration space method, the range of possible positions for N degrees of freedom are parameterized as an N-dimensional space, and solved numerically. The configuration space for a robot of arbitrary dimension may be calculated *a priori*, and navigated using any of a number of path planning algorithms[23] [24]. Since the Canfield has three degrees of freedom, its configuration space may be rendered as a cube with opposing faces identified, as shown in Figure 3.11. Some parts of the cube must be eliminated to account for self-intersection: for example, the joint angles cannot wrap all the way around without the legs colliding with the distal plate. The singularities found in Section 3.4 should be treated as obstacles to be avoided.

3.6 2 DoF Operation

Orientation requires only two degrees of freedom. The Canfield has three, so infinite solutions exist for a given orientation. This may be illustrated with the trivial example of the plunge test undertaken in Section 4.5: the height of the distal plate is changed with plunge distance, but the orientation remains the same. One way to restrict the inverse kinematics problem to two degrees of freedom is to maintain a constant plunge distance. This "plunge sphere" forms a surface in the configuration space, and may be selected to minimize singularities.

A likely failure mode for the Canfield is a scenario in which one leg is frozen. The configuration space in this case becomes a two-dimensional slice of the cube in Figure 3.11.

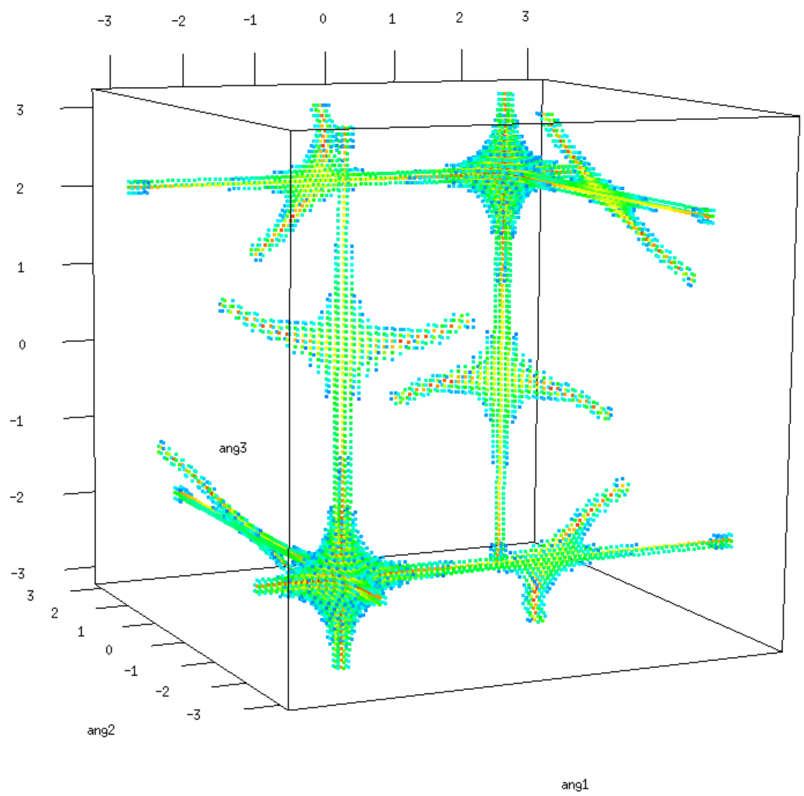

Figure 3.11. 3D map of the configuration space, with midplane singularities highlighted. Image credit: Christian Bueno.

3.7 Base/Leg Ratio

Canfield defines[6] the ratio $R_b = b/l$, where b is the length of the base and l the length of one leg member, and notes its effect on the size of the workspace. The following analysis, however, demonstrates that this ratio exists in three regimes, discoverable by an analysis of how the midpoints of each joint relate to the center of the linkage, based on the tipi configuration shown in Figure 3.7.

In order to have the midpoint and center align, the triangle formed by the center of the joint, center of the base, and the base hinge must be such that hypoteneuse has length l. The distance from the base center to base hinge is $\frac{b}{\sqrt{3}}$, returning the angle $\pi - \theta_i = \arccos(b/\ell\sqrt{3}) \implies \theta_i = \pi - \arccos(b/\ell\sqrt{3})$.

This yields three regimes. When $\ell < b/\sqrt{3}$, this angle is undefined, implying that the tipi configuration cannot be achieved. This forms the "Short Regime". The transition appears when $\ell = b/\sqrt{3}$, and $\theta_i = \pi - \arccos(1) = \pi$, where the arms touch at the center of the base plate; the "critical regime." When $\ell > b/\sqrt{3}$, the tipi configuration becomes achievable. This is termed the "Dragon Regime," which exhibits significantly more singularities[3] in its configuration space. The joint ratios are illustrated in Figure 3.12.

Table 3.2. Table of base/length ratio regimes.

Ratio	**Regime**
$l < b/\sqrt{(3)}$	Short Leg
$l = b/\sqrt{(3)}$	Critical
$l > b/\sqrt{(3)}$	Dragon

There is a tradeoff between the regimes: Although the long-legged dragon regime has many singular configurations, it also boasts the largest workspace. The prototype joint in Chapter 4, as shown in the dimensioned drawing in Figure 3.13, has a base length of 10 and a leg length of 18, placing it firmly in the dragon regime.

Canfield's original prototype[22] has a ratio on the order of $R_b = 0.75$[6], which enables its large hemispherical workspace.

The tradeoff between singularities and workspace may be illustrated through the *reductio ad absurdum* example of a Canfield joint with very large plates and short legs: It cannot become singular, but its workspace is extremely restricted.

[3] "Here there be dragons."

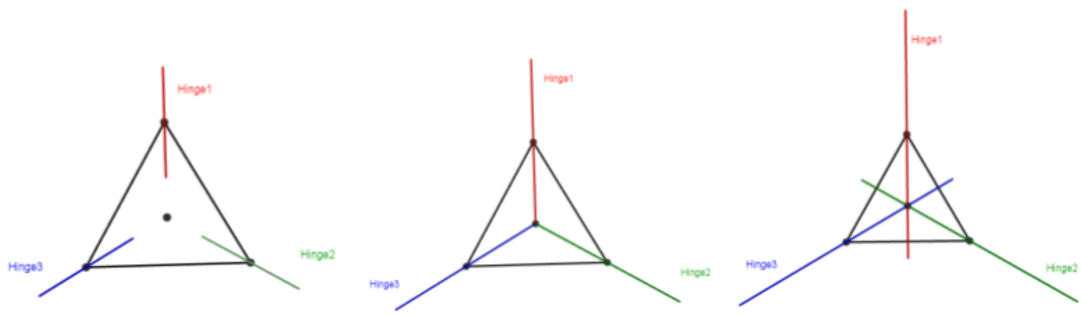

Figure 3.12. Illustration of regimes. Image credit: Robert Short.

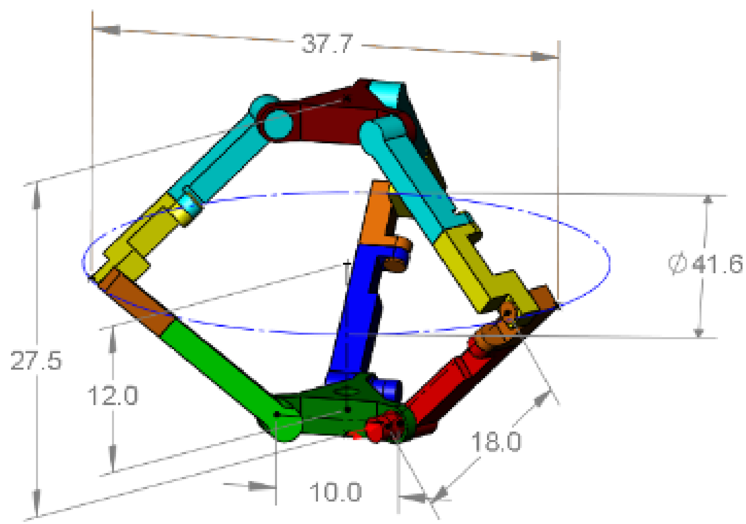

Figure 3.13. Dimensioned drawing of prototype joint. Image credit: Balcones.

3.8 Future Work

This chapter represents the current state of kinematic analysis of the Canfield joint. Much theoretical work remains to be done, especially from a topological robotics perspective. Further analysis of the Canfield joint as a kinematotropic linkage (Section

3.4) is currently underway. The same is true of the base/leg length regimes and their respective workspaces and load capacities, which may recommend the different regimes for specific purposes. For applied use, it is imperative to ensure that the set of singularities is complete — or, at least, that the configuration space map is sufficient to ensure singularity-free operation. Some singularities, such as the leg lock, require further examination. Software control may be sufficient to keep the joint from entering singular configurations, but it may be worthwhile to examine the option of adding mechanical stops for this purpose. Once the safe paths through the configuration space are known, it will be necessary to implement controls for the prototype, likely using the techniques developed in Section 3.5. Verification of a complete singularity-free tracking trajectory (e.g., Mars to Earth for an extended period, per the existing simulated trajectory[25]), both for a fully functional joint and for a damaged joint with a frozen leg at various angles, is a logical next step.

4 Validation of Prototype Canfield Joint

4.1 Prototype

A prototype version of the Canfield joint for the iROC project, shown in Figure 4.1, was custom fabricated by Balcones Technologies of Austin, Texas. A labeled rendering of this prototype is shown in Figure 4.2, and a screenshot of its control interface is shown in Figure 4.3. The primary experimental component of this work is comprised of optical metrology and inertial measurement used to validate this prototype for the project specifications.

4.2 Mission Description

The pointing requirements used for validation are based on a use case of a Mars orbiter communicating optically with a Deep Space Network (DSN) receiver on Earth, as shown in Figure 4.4. The orbiter circles Mars with a downward-facing camera, and its coordinate frame is defined as shown in Figure 4.5. The pointing requirements used in this validation were found by simulation[25].

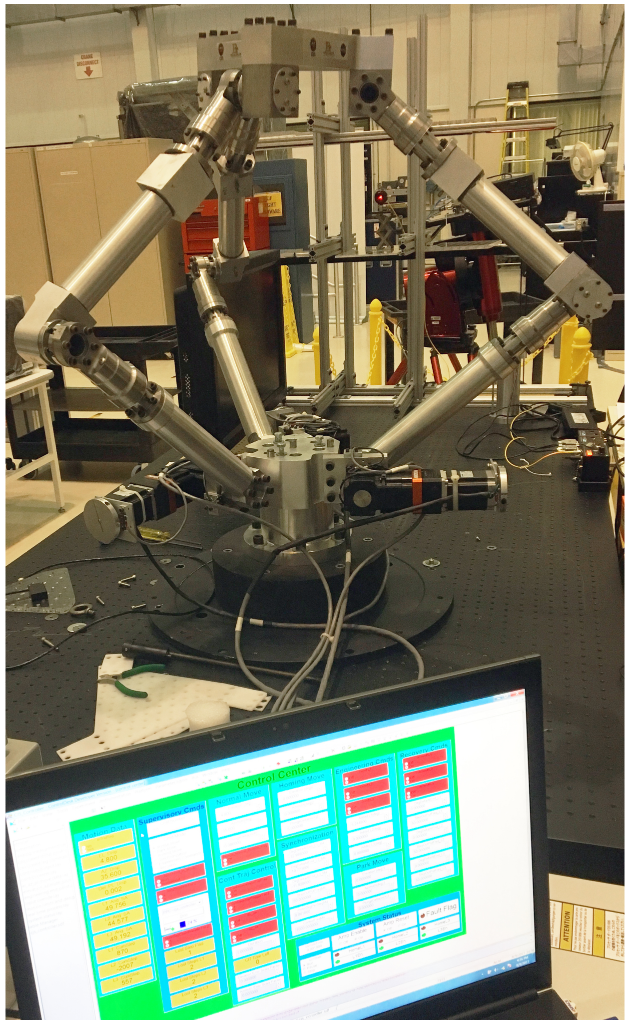

Figure 4.1. Prototype Canfield joint, with metrology tower in background. Photo credit: Daniel Raible.

4.3 Validation and Benchmarking Objectives

Several tests were devised to assess the prototype's performance according to the mission requirements. These are summarized in Table 4.2.

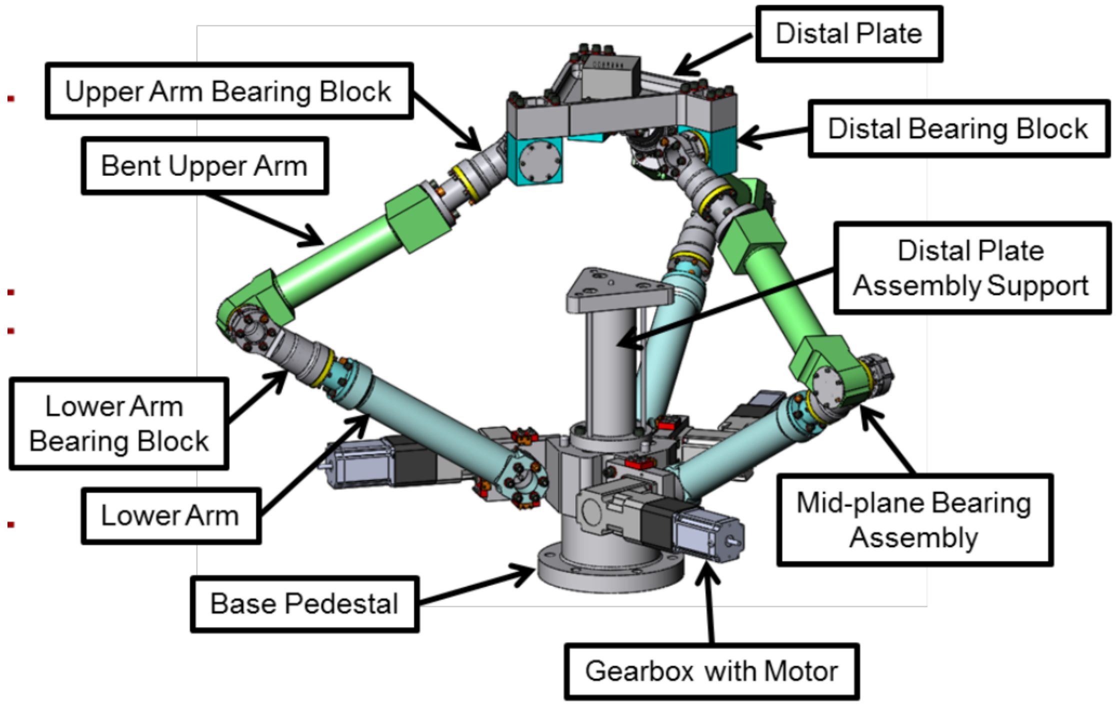

Figure 4.2. Parts of prototype joint. For the purposes of these tests, the distal plate assembly support was removed. Image credit: Balcones.

4.3.1 Field of Regard

Disambiguation. A distinction is emphasized between the field of view of the quad detector in the optical metrology system described in Section 4.4.3, and the field of regard (angular coverage) of the robot itself. The latter was verified by inspection to fit the project requirements of 330 degrees in azimuth and ±83 degrees in elevation.[25][1] The former was found in Section 4.6.

[1]Per simulation, the azimuth range is 14.55° to 345.45°, and the elevation range is -82.41° to 82.48°.

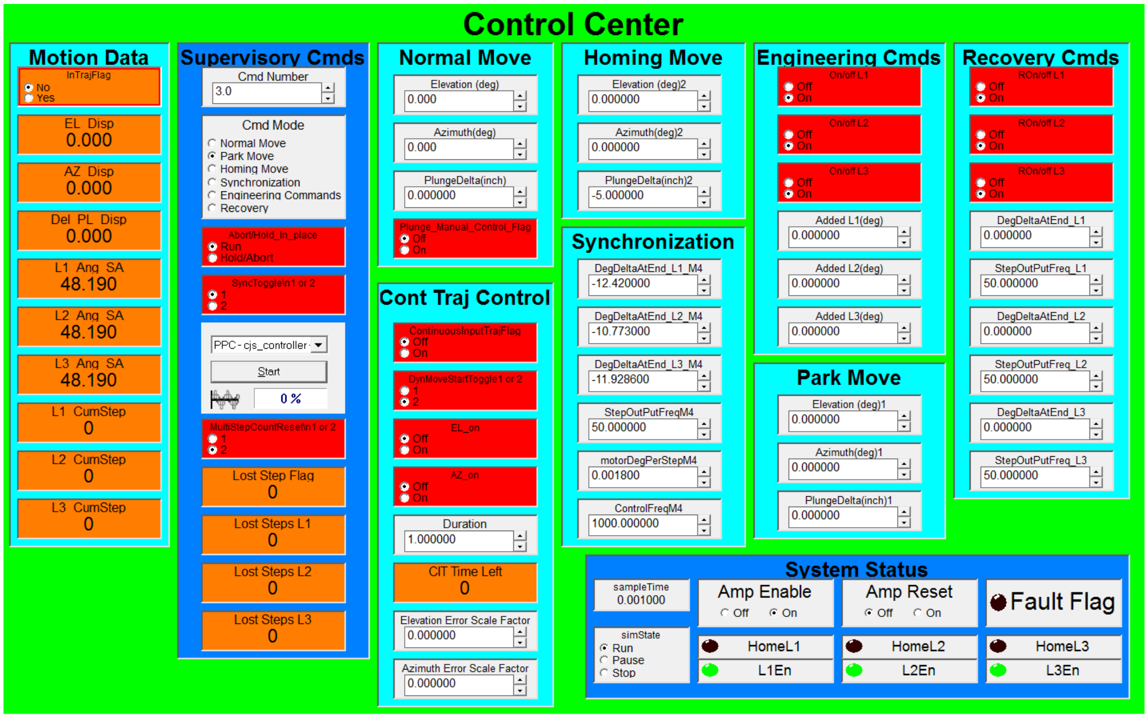

Figure 4.3. Control interface for prototype joint.

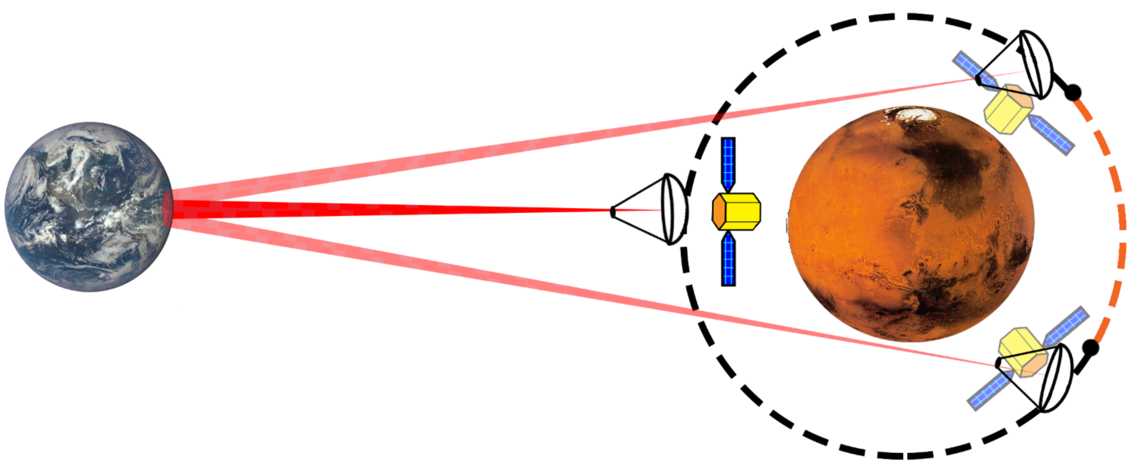

Figure 4.4. Mission illustration.

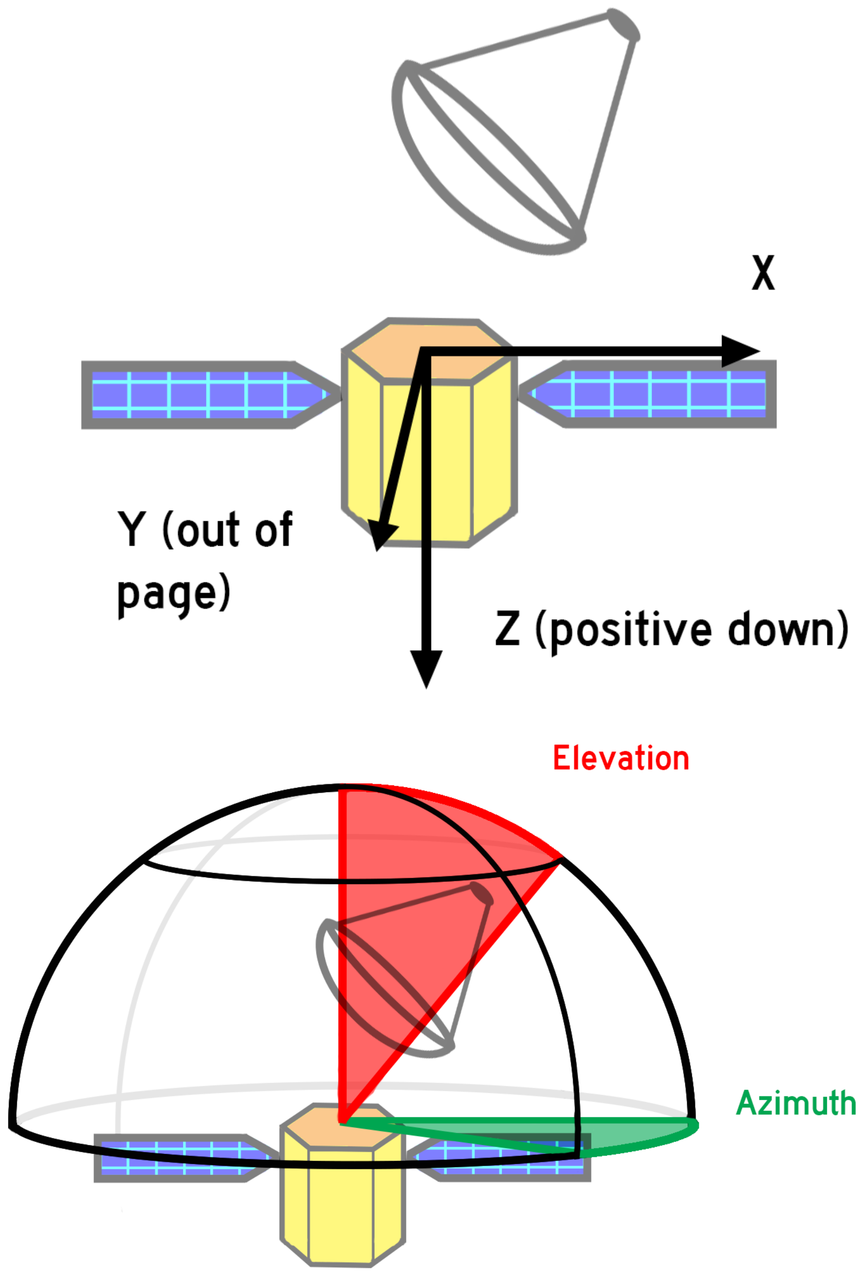

Figure 4.5. Illustration of reference frame for spacecraft, teletenna.

4.3.2 Resolution (Step Size)

The term "resolution" is used here to describe the smallest commanded move the prototype is capable of executing. This appears to be chiefly subject to stiction effects, and was assessed by the stiction test described in Section 4.7. The resolution is determined by the receiver: As shown in Figure 4.6, the width of an acceptably attenuated (3dB) beam projected toward Earth is traced to a subtended angle in the coordinate frame of the spacecraft. In the iROC link budget, a step size of 0.0025° (25 μradians) is required.[1]

4.3.3 Slew Rate

The slew rate — the rate of angular movement projected onto a horizontal plane — is considered here in the sense in which it is defined in astronomy. This must be measured in azimuth and elevation, and both short and long duration moves. Since the prototype is driven by stepper motors, long-duration moves are limited by its velocity characteristics, while short-duration moves are limited by its acceleration characteristics. A maximum slew rate of 0.5 degrees per second is required[1] when the orbiter passes in the shadown of the planet and the teletenna must be returned to its starting position for the next pass, as shown in Figure 4.4. During the main part of the orbit, when the teletenna is pointed toward Earth, a slower slew rate is required.

4.3.4 Repeatability

As with angular slew rate, the repeatability is affected by the length of moves: small moves are subject to stiction effects, and longer moves may accumulate errors from lost steps. Accumulated errors, left uncorrected, could compromise tracking capability. The short range repeatability was examined in the field of view test described in Section 4.6, and the long range repeatability test is described in Section 4.8. Per

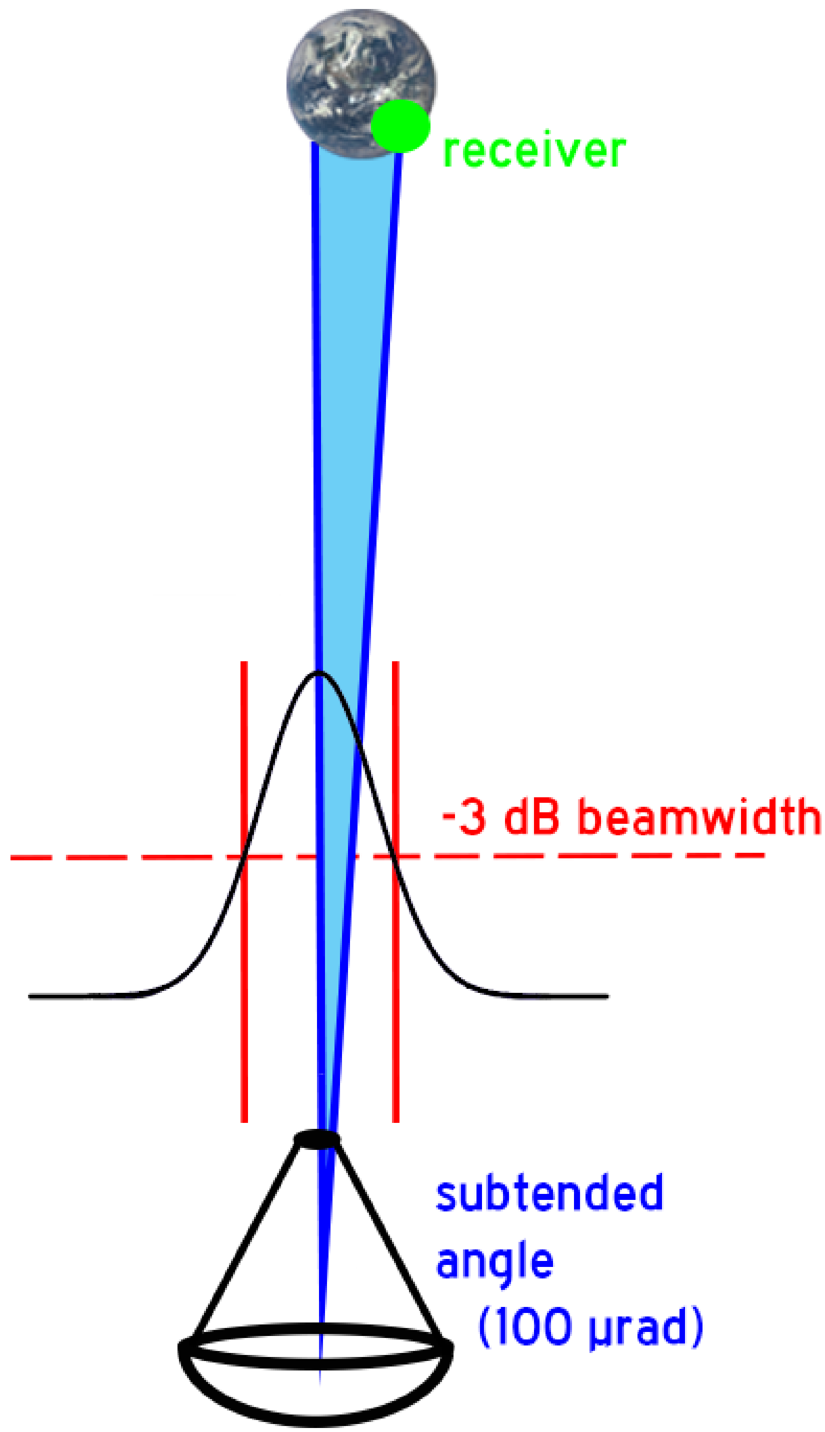

Figure 4.6. Illustration of attenuated beam width. The blue angle represents the absolute pointing precision of 100 μradians.

the subtended angle analysis described in Section 4.3.2, absolute pointing precision of 0.006 degrees (100 μradians) is required.[1]

4.3.5 Disturbance Characteristics

Exploration of the prototype's vibration characteristics is outside the main scope of this work, but the data collection system outlined in Section 4.4.2 does pick up small disturbances. Vibration data is of interest for future testing. The MEMS sensors used to collect position data may have too high a noise floor to collect a meaningful estimate of the power spectral density, so adding piezoelectric accelerometers to collect low frequency data is advisable in future work.

4.4 Metrology Apparatus

The movement of the distal plate was characterized by optical metrology, as well as by the position feedback of the robot's servos.

4.4.1 Mounting System

The quad detector and inertial measurement apparatus were mounted to the distal plate of the prototype, using a laser-cut adapter plate, as shown in Figure 4.8. The adapter plate was designed from the dimensioned drawing shown in Figure 4.7, with holes spaced according to imperial optical table convention.

The laser was mounted to a tower built from 80/20 mounting rail on the far side of the optical table, shown in Figure 4.1.

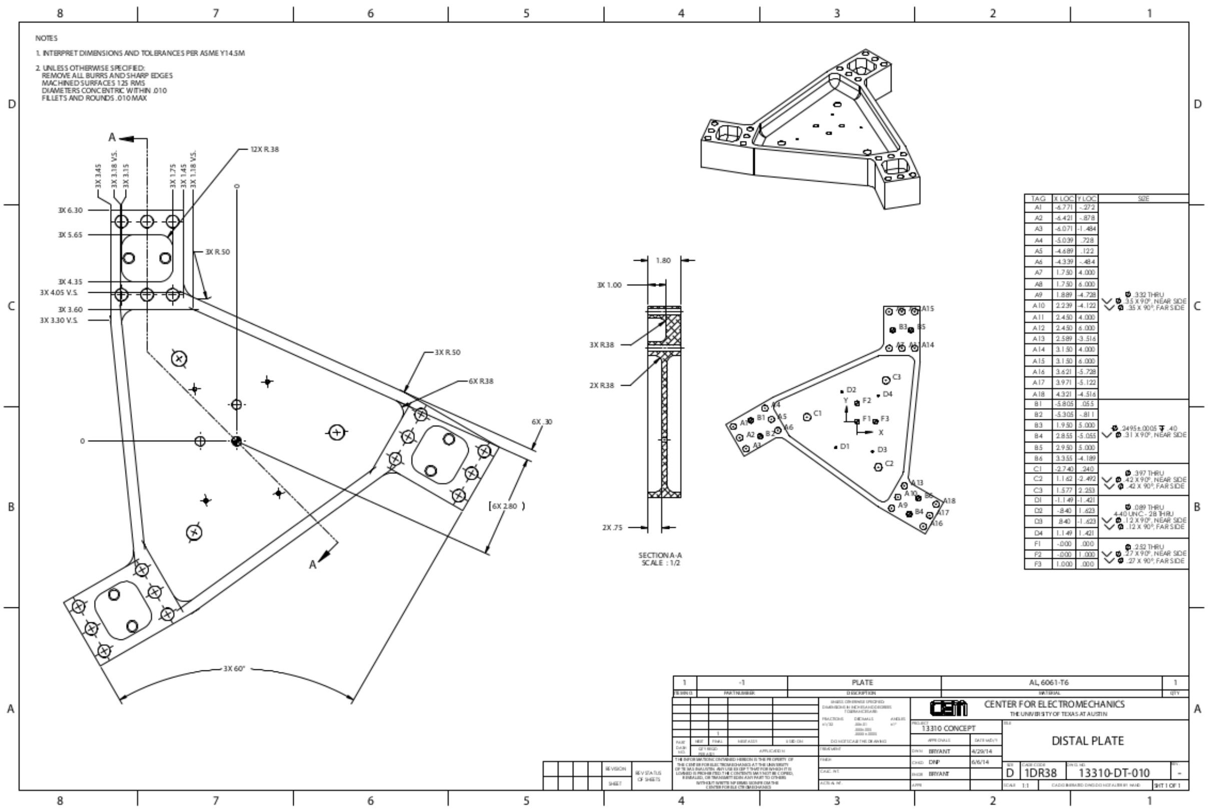

Figure 4.7. Dimensioned drawing of distal plate. Image credit: Balcones.

4.4.2 Inertial Measurement

Due to equipment availability constraints, a Motorola Droid Razr HD cellular phone was used in place of an inertial measurement unit. In each test, the outputs of its accelerometers were recorded as .csv files, as shown in Figure 4.9. The phone uses three InvenSense MPU6050 accelerometers.

4.4.3 Optical Metrology

The parts of the optical metrology apparatus are listed in Table 4.1.

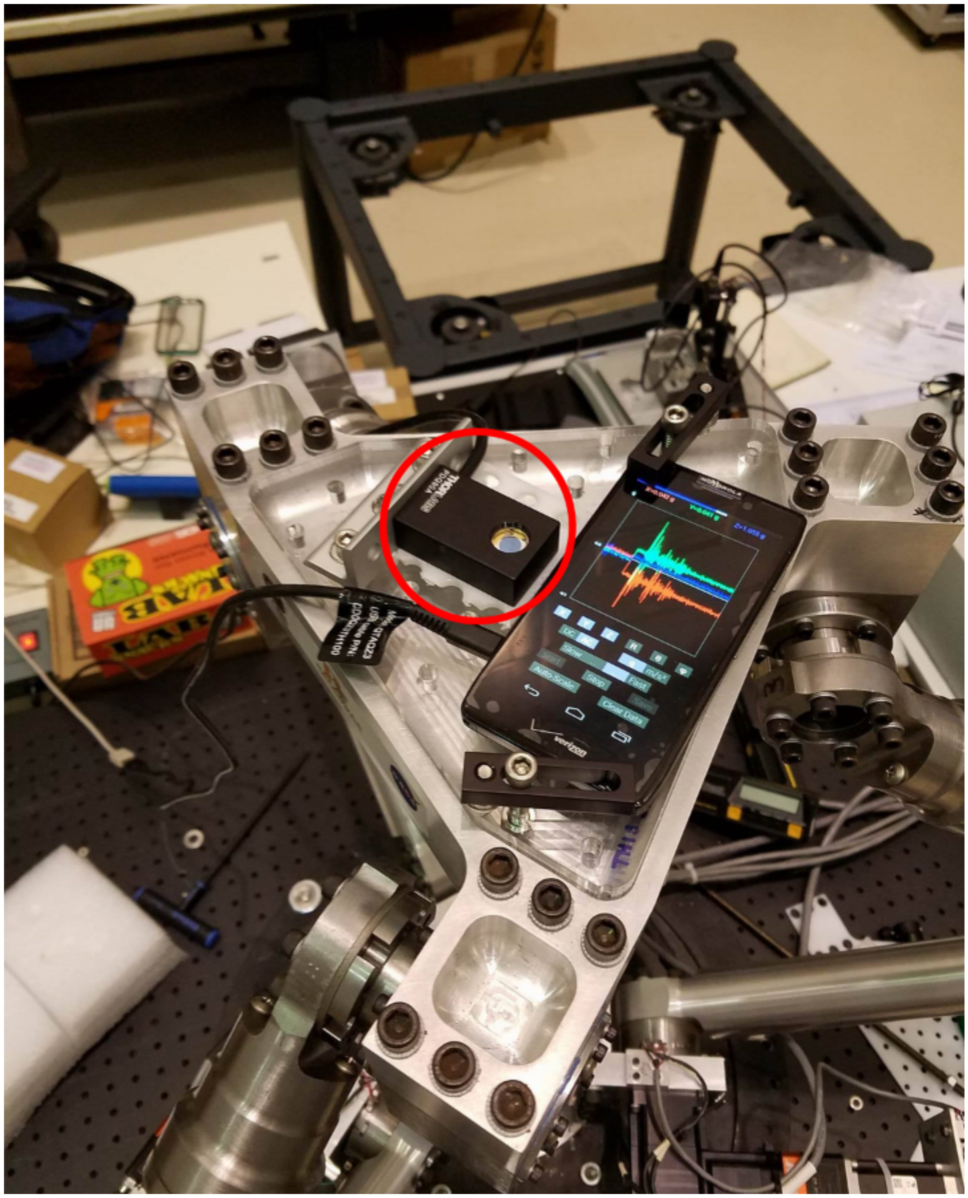

Figure 4.8. Photograph of cell phone and quad detector (circled) mounted parallel to distal plate.

The optical data was collected from a PDQ80 quad detector using a KPA101 interface control, which was connected to a computer via the KCH601 USB hub.[2] Data was recorded using the ActiveX controls in MATLAB, included in Appendix A.

[2]A HIROSE extension cable, not listed in Table 4.1, was fabricated to connect the detector to the USB hub.

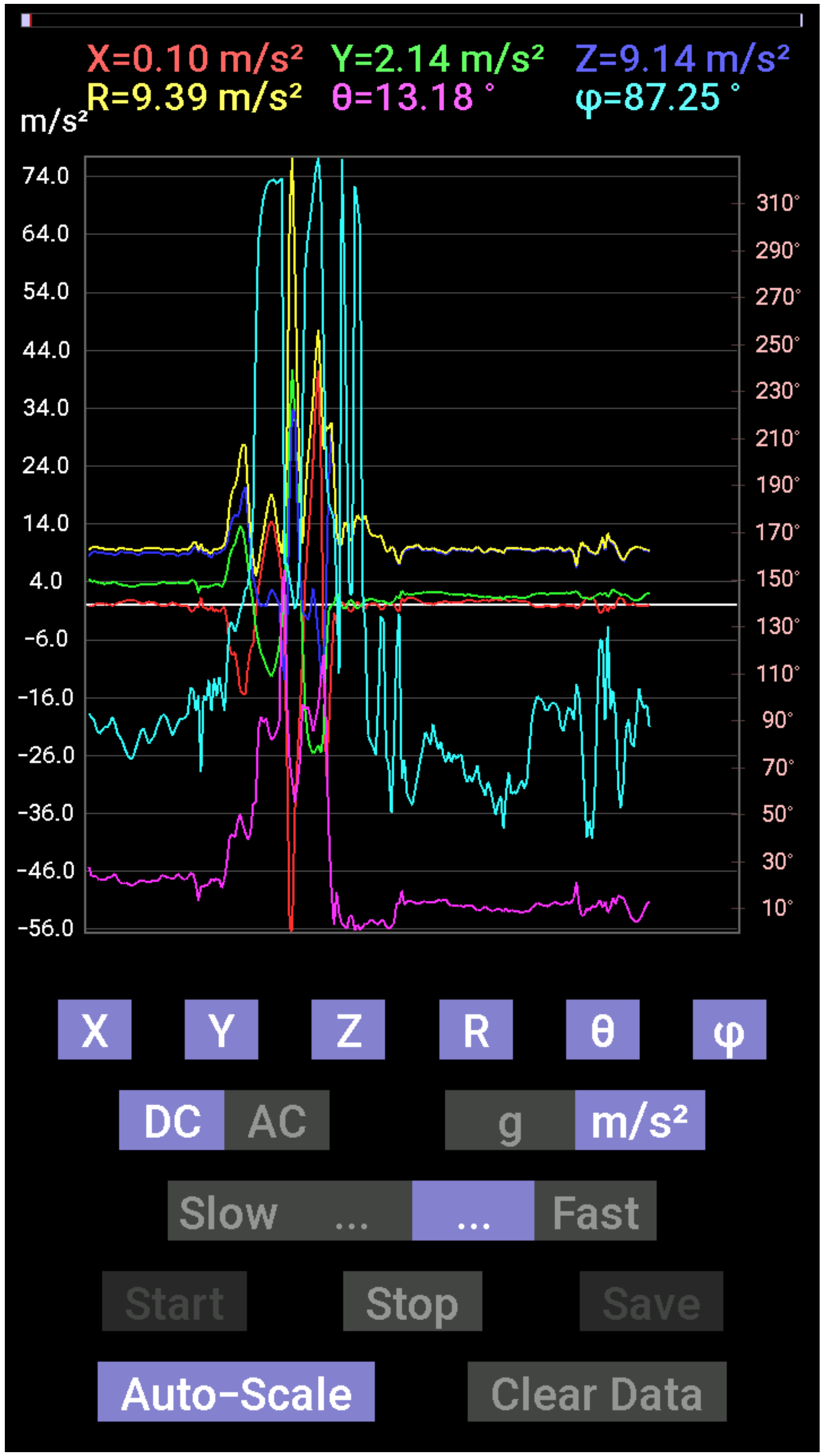

Figure 4.9. An example screenshot from the application[3] used to record position and orientation data.

Table 4.1. Bill of materials for optical metrology apparatus.

ThorLabs Part	**Part Description**	**Price**	**Notes**
PDQ80A	Quadrant Detector Sensor Head	$490.00	400-1050 nm
TLS001-635	T-Cube Laser Source	$1135.00	635 nm, 4.0 mW max
KCH601	USB Controller Hub and Power Supply	$587.00	
KAP102	Adapter Plate for 120 mm T-Cubes	$61.25	
KPA101	K-Cube Position Sensing Detector Auto-Aligner	$789.00	
P1-630A-FC-2	Single Mode Fiber Patch Cable	$69.75	2 m, 633-780 nm, FC/PC
CFC-11X-A	Adjustable FC/PC Collimator	$258.00	f=11.0 mm, ARC 350-700 nm
KST101	K-Cube Stepper Motor Controller	$626.00	

4.5 Plunge Distance Test

In the plunge test, the distal plate was moved up and down along the robot's vertical axis, with no variation in azimuth. This test, illustrated in Figure 4.10, provided a simple first pass for running the instrumentation, and a qualitative initial test of repeatability.

4.5.1 Methodology

The quad detector was mounted perpendicular to the plate for this particular test. The distal plate was held level while the plunge distance was varied from -10''to

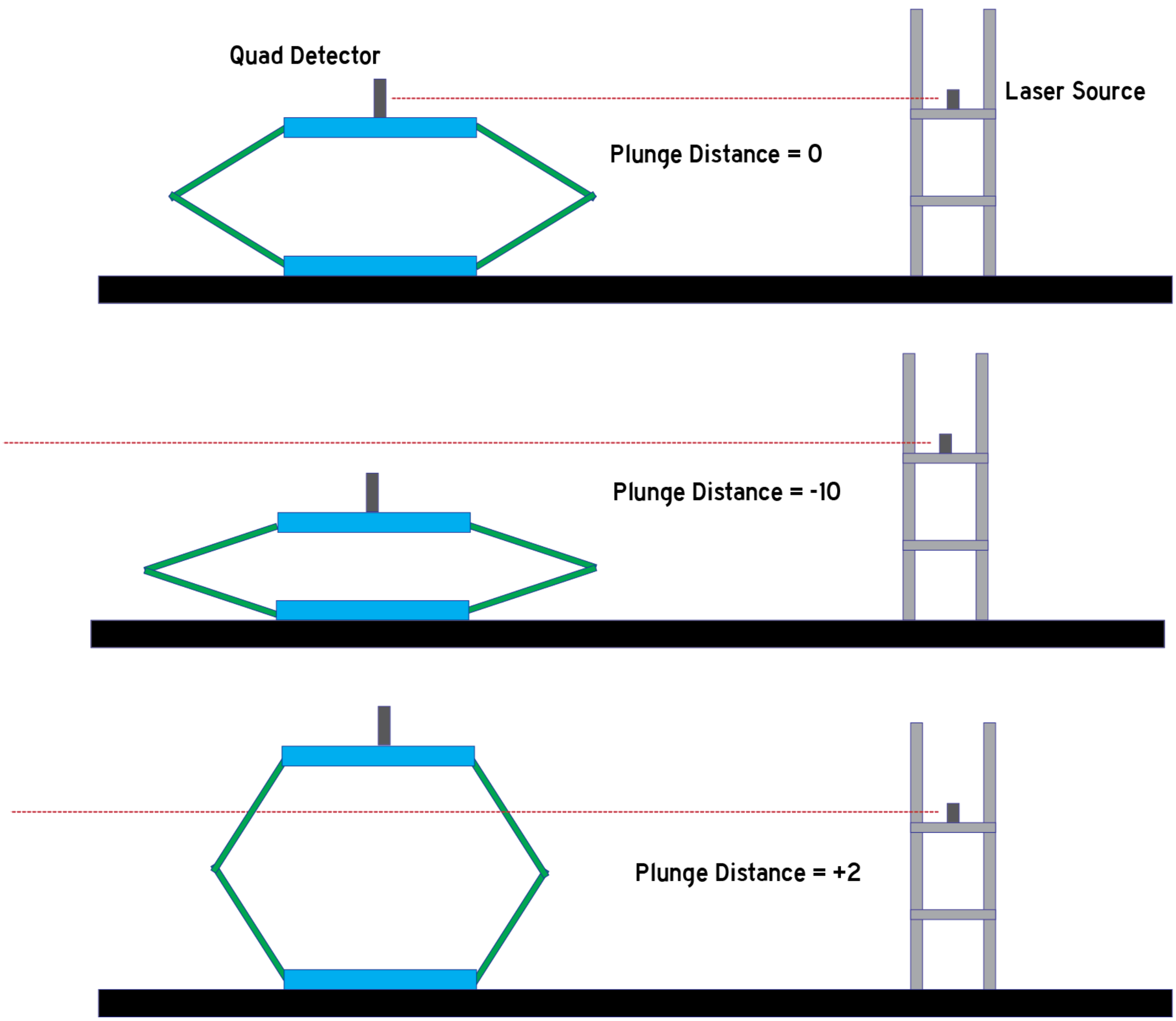

Figure 4.10. Illustration of plunge test.

+2''and back. The laser dot crossed the surface of the quad detector from top to bottom.

4.5.2 Results

The optical data from this test is plotted in Figure 4.11. This test served to gather data on the plunge rate, as well as to provide some qualitative preliminary data on

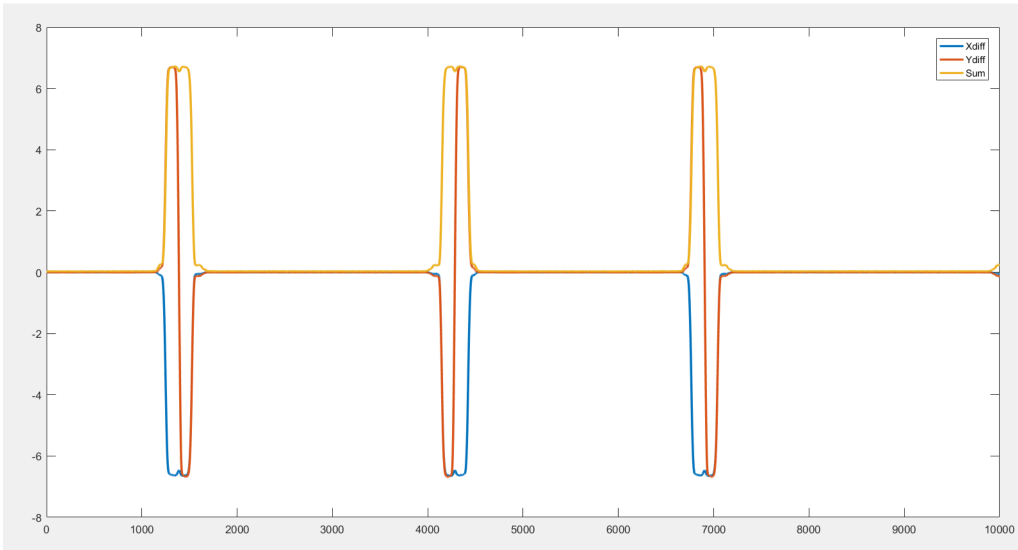

Figure 4.11. Optical results from plunge test. This plot shows the output of the detector as the laser dot moves past the detector from top to bottom, bottom to top, and back again over 10,000 samples.

repeatability and resolution. Once the data from both sensors was integrated and parity between these data sets was confirmed, it was possible to develop and execute the more complicated tests that follow.

4.6 Field of View Test

This test was used to gather data on slew rate via the optical metrology system.

4.6.1 Field of View Calibration

In order to relate the data collected by the optical system to the movement of the distal plate, it was necessary to assess the field of view of the optical system, i.e., the angular range eclipsed by the surface of the quad detector, relative to the position feedback from the robot's servo system.

Since the longest path possible across the surface of the detector is the diagonal path, the joint was positioned such that the laser aligned with the lower left corner of the quad detector. This point (azimuth of 170°, elevation of 72°) was recorded. The point where the laser dot aligned with the upper right corner of the detector (azimuth of 170°, elevation of 75°) was also recorded. The test procedure is illustrated in Figure 4.12.

The PDQ80 has an active area of 8 mm x 8 mm. By the distance formula, the length of the diagonal is $\sqrt{(8^2 + 8^2)} = 11.3$ mm, which, as tested above, maps to 2.5° of the joint's field of view. The resolution of the optical system, therefore, is .22 degrees per mm on the detector, a relation which holds as long as the plunge sphere remains constant.

4.6.2 Slew Rate Measurement

The joint was given a trajectory from one point to the other, and optical data was collected. To check for short-range repeatability, it was sent back to the original position, and then repeated several times with a trajectory of a constant 170° in azimuth and 73 to 74.25° in elevation. The trace of the laser dot on the quad detector is shown in Figure 4.13. The slew rate may be calculated from this test by taking the derivative of the distance traveled along the trajectory, according to the optical system, with respect to time. This returns maximum values of 15-20 mm/s, indicating a slew rate of approximately 3 degrees per second, comfortably above the 0.5 degrees per second required.

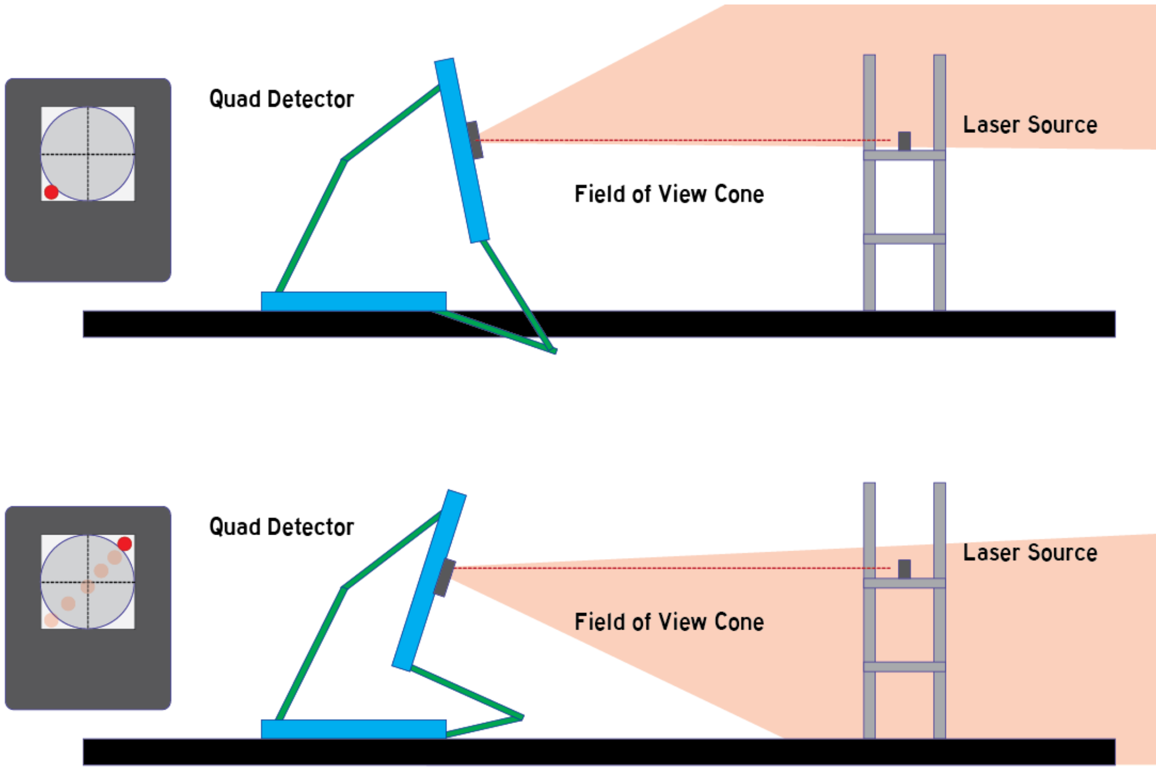

Figure 4.12. Illustration of field of view test. The object of the test is to measure the width of the cone with respect to the laser source.

4.7 Stiction Test

This test was used to determine the minimum step size and the effects of stiction on short-range repeatability.

4.7.1 Methodology

In this test, the joint was pointed such that the laser dot was centered on the detector, as shown in Figure 4.15. The robot was then commanded to move one step forward in a direction (azimuth or elevation), then back to the original position, then two steps forward, then back, then three steps forward, and so on. The optical and

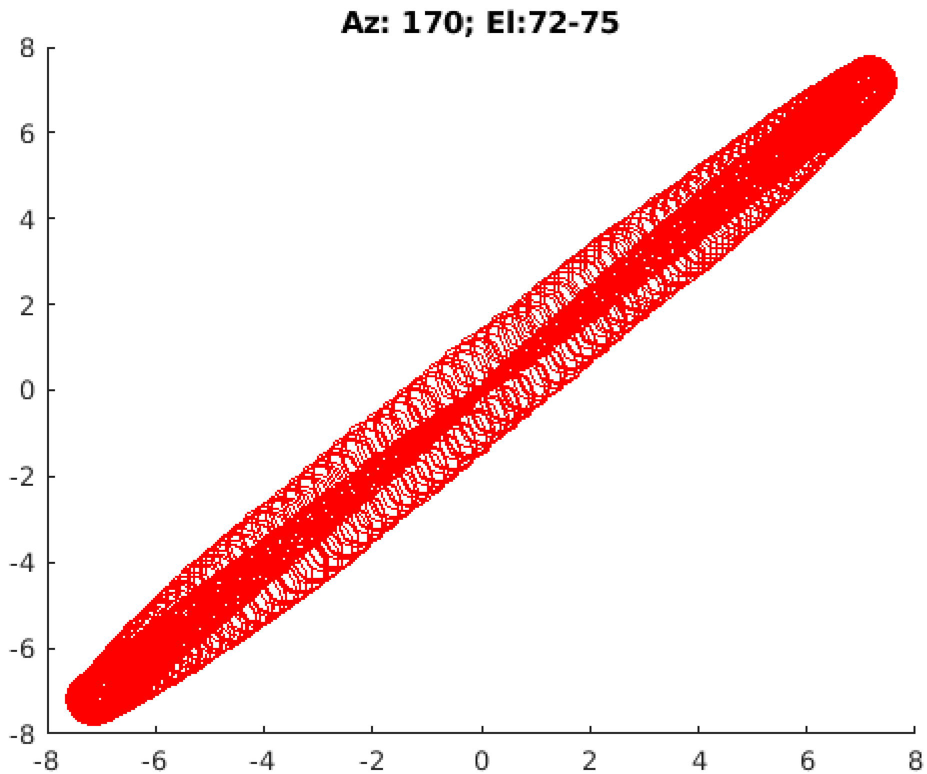

Figure 4.13. Optical metrology data from the field of view test. The area of the plot corresponds to the 8 mm x 8 mm area of the quad detector. Several passes across the detector over time are represented.

accelerometer data were retained in order to measure the actual movement of the robot. This test is illustrated in Figure 4.14.

4.7.2 Results

The test was performed twice: once in azimuth, once in elevation. Results are shown in Figures 4.16 and 4.17. A horizontal line on each plot indicates the initial value, to which the output should, ideally, return. However, accumulated drift on the scale of millimeters (and therefore degrees) is shown. Slew rate for these short duration moves, calculated using the same method described in Section 4.6.1, is on the order of 0.5

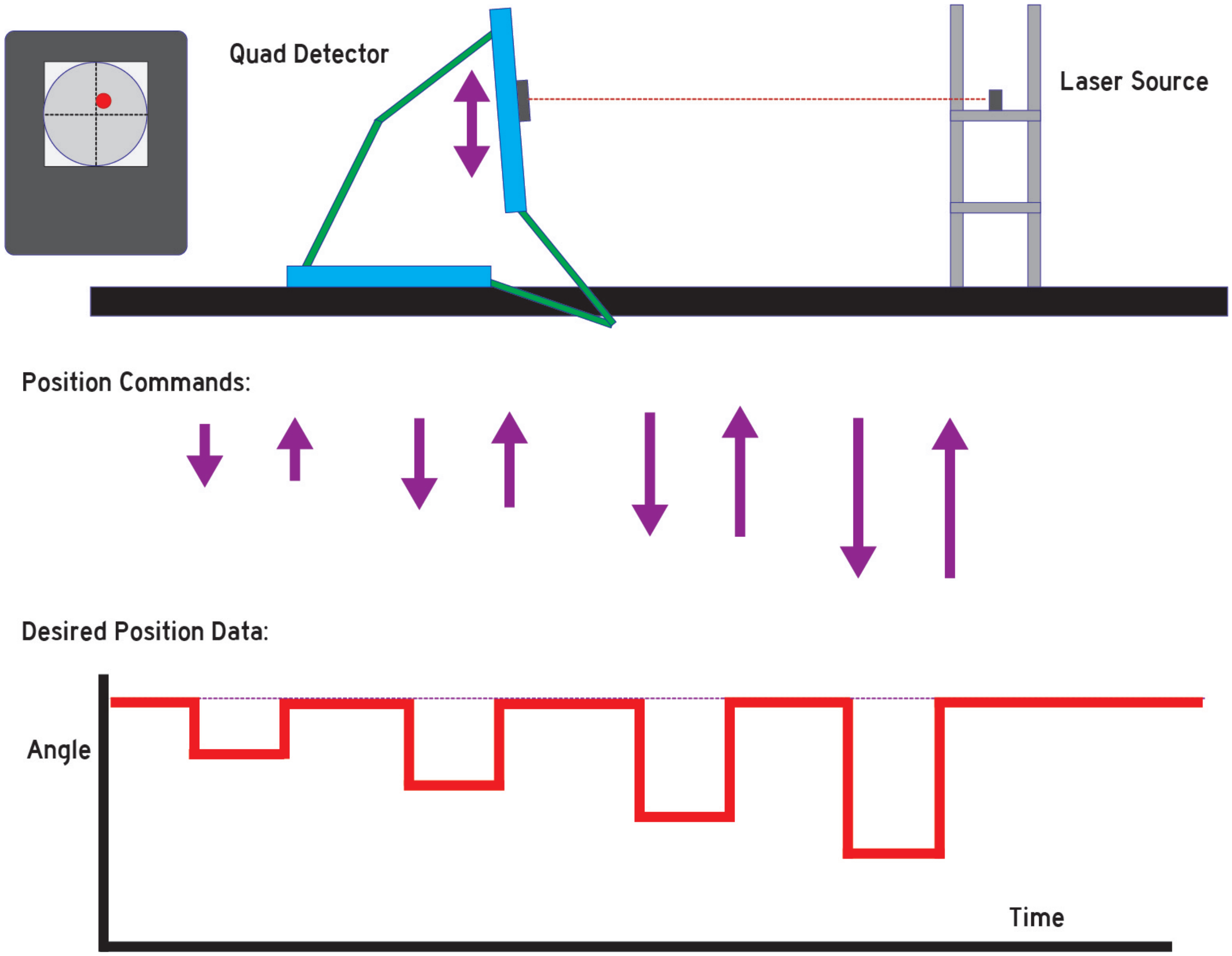

Figure 4.14. Illustration of stiction test.

degrees/second. The resolution was also verified in this test: a single step, as defined by the control interface, affects the position of the joint, and is not overwhelmed by stiction effects.

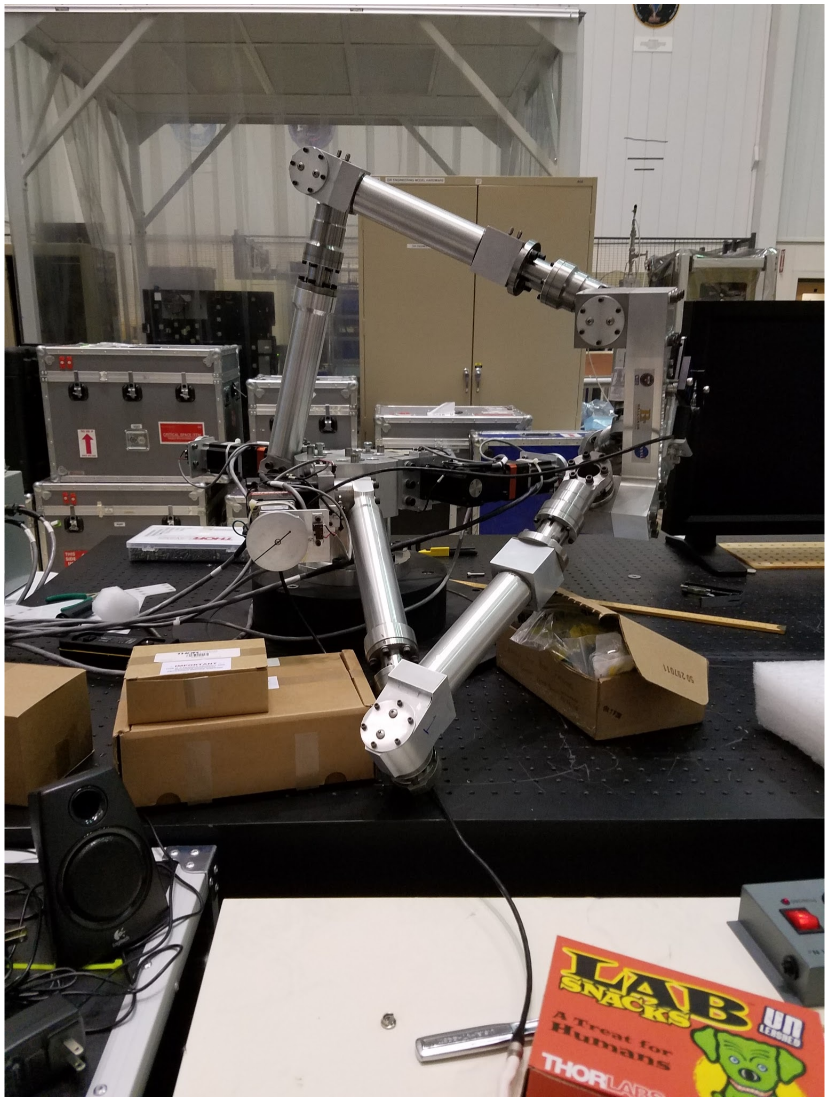

Figure 4.15. Joint orientation to align laser dot with detector, as used in the stiction and field of view tests.

4.8 Long-Range Repeatability Test

4.8.1 Methodology

To test long-range repeatability, the joint was positioned to center the laser dot on the detector. Commands were then sent to move the joint an arbitrary distance away

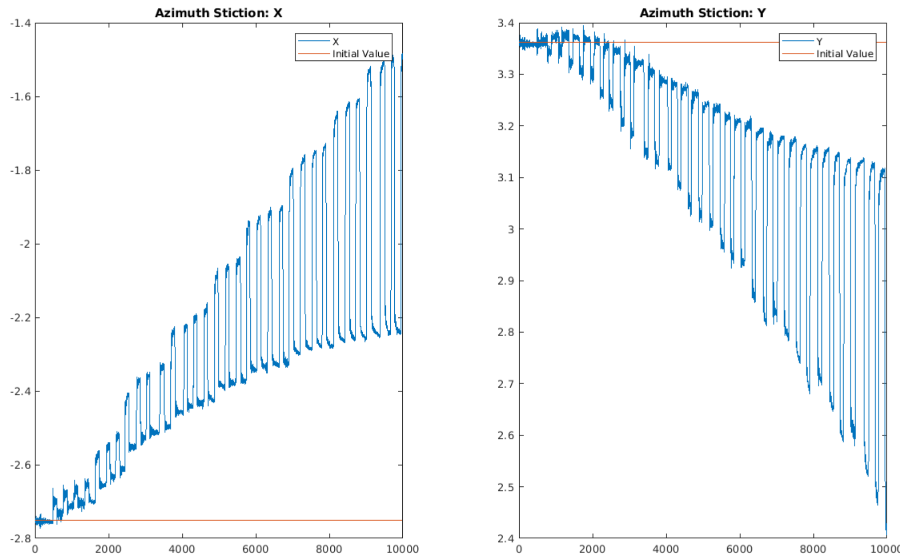

Figure 4.16. IMU results from azimuthal stiction test. The horizontal axes are the number of samples, and the vertical axes are in degrees.

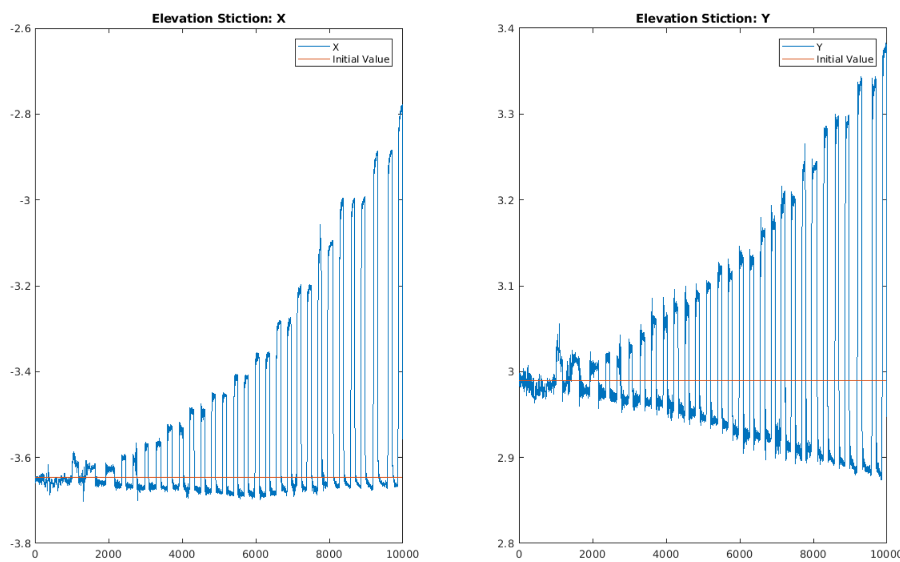

Figure 4.17. IMU results from elevation stiction test. The horizontal axes are the number of samples, and the vertical axes are in degrees.

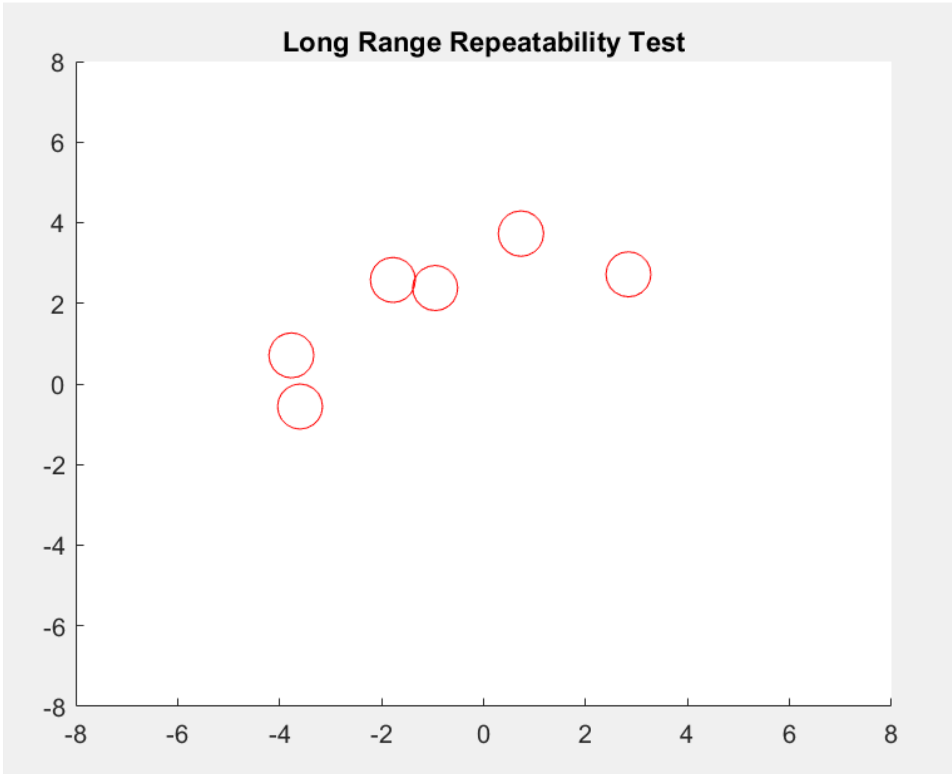

Figure 4.18. Optical results from long range repeatability test. Each dot represents the position of the laser on the quad detector after a long trajectory.

and back again. The position of the dot on the detector was recorded manually after each trajectory.

4.8.2 Results

The resulting data points are shown in Figure 4.18. The two dots for this test farthest from one another, at (-3.6, -.56) and (2.84, 2.72), have a distance of 7.2 mm between them on the detector, which, by the field of view calibration performed in Section 4.6.1, indicates a significant drift of 1.6°. This demonstrates that accumulated errors may compromise long-range repeatability.

Table 4.2. Review of pointing requirements and relevant validation procedures for Mars orbiter use case.

Specification	**Requirement**	**Test**	**Result**
Field of Regard (Angular Coverage)	330° AZ, ±83° EL	By inspection	✓
Resolution (Step Size)	0.0025°	Stiction test	✓
Slew Rate	0.5°/sec	Field of view test	✓
Pointing Precision	0.006°	Repeatability test	X

4.9 Mechanical Failure

Data collection was interrupted during the long range repeatability test by a mechanical failure: the gearbox on one of the legs underwent a sudden shear fracture, stripping one of the gears. This was likely a result of backlash produced by the robot entering and leaving the leg lock singularity described in Section 3.4.2.

4.10 Conclusion

The prototype Canfield joint met the requirements for field of regard, step resolution and slew rate, but has not been validated with regard to short or long range repeatability. The considerable drift which appeared in the repeatability tests precludes validation of the pointing precision requirement at this stage.

Because of the failed gearbox, it is necessary to undertake these tests again after the prototype is repaired. Possible improvements to the experimental apparatus at that time include implementing synchronized data collection between the optical and inertial sensors and automating the tests on the robot's controller. The long-range repeatability test should be performed with a larger number of data points, and the stiction test should be performed with both incrementing and decrementing parameters in order to examine the effect of sag. Ultimately, the backlash which caused the failure of the gearbox should be quantified and addressed by the control system.

5 Physical and Virtual Models

The kinematic analysis work discussed in Chapter 3 was largely performed through discussions in a collaborative environment. The utility of a desktop physical model quickly became apparent. Three physical models were constructed in the course of this research: a 3D-printed replica of the original prototype and two LEGO models. For the reader, details of each model are provided herein for future use.

5.0.1 Additive Prototype

A 3D-printed replica of the original prototype used by Canfield [6] was fabricated on a Makerbot Replicator at CWRU's think[box] facility and a Fortus 250mc 3D printer at NASA Glenn, as shown in Figure 5.2. The model was reconstructed from the drawings of Anthony Ganino [22], and printed in PLA and ABS plastic. The 3D-printed structure is shown in Figure 5.1. The parts were printed separately and assembled; an example of printed parts is shown in Figure 5.2. The parts are held together with metal fasteners, but the relatively poor tolerances in the print make the model difficult to actuate. In future revisions, the fasteners may be integrated into the design through the use of a dissolvable support material, enabling the constructed linkage to be produced in a single print. This would make the robot scaleable, and would represent a first step toward producing Canfield joints in operational environments through additive manufacturing.

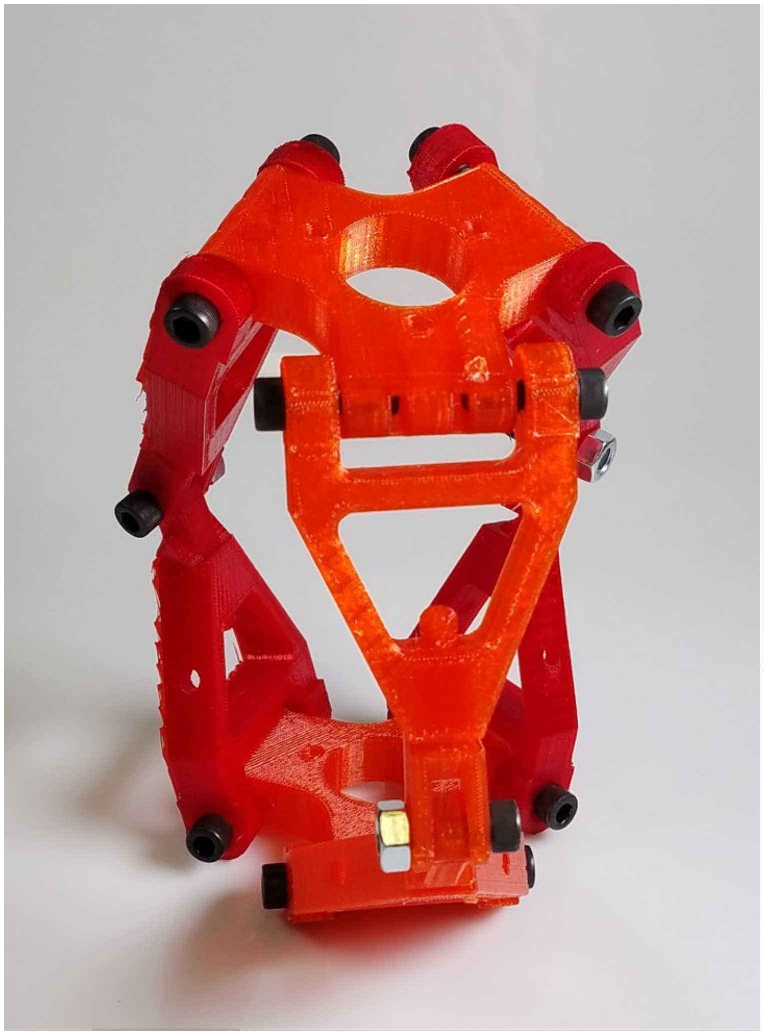

Figure 5.1. 3D printed replica of original prototype, printed in PLA at think[box].

5.1 LEGO Models

The utility of LEGO bricks has long been recognized in the robotics community: LEGO models are straightforward, cost-effective, and easily modified to vary proportions. They translate naturally to the educational sphere, helping students develop

Figure 5.2. Parts for 3D-printed replica, printed in ABS at NASA Glenn.

an understanding of modularity, part numbering, and the construction of a bill of materials.

5.1.1 Basic LEGO Model

The first revision of the LEGO model, shown in Figure 5.3, whose bill of materials is listed below, can be purchased from the LEGO replacement brick service for about $10. Instructions for its construction are appended. This model uses two ball joints to approximate the hinges at each elbow and the revolute joints between the elbows and legs; as such, it has a greater range of freedom than the actual joint, but can be used to illustrate poses.

5.1.2 LEGO Technics Model

LEGO Technics are a series of LEGO parts, compatible with standard bricks, that are intended to model realistic technical functions. This model, shown in Figure 5.4, has the correct arrangement of joints for each leg, although the plate joints' range is

Table 5.1. Bill of materials for basic LEGO model.

LEGO Part #	**Part Description**	**Quantity**
3795	2x6 Flat	18
11476	Hinge A	6
48336	Hinge B	6
14704	Ball Joint A	18
14417	Ball Joint B	18

Figure 5.3. The design of the basic LEGO joint model.

limited. It has smoother movement and more nearly resembles the prototype tested in Chapter 4.

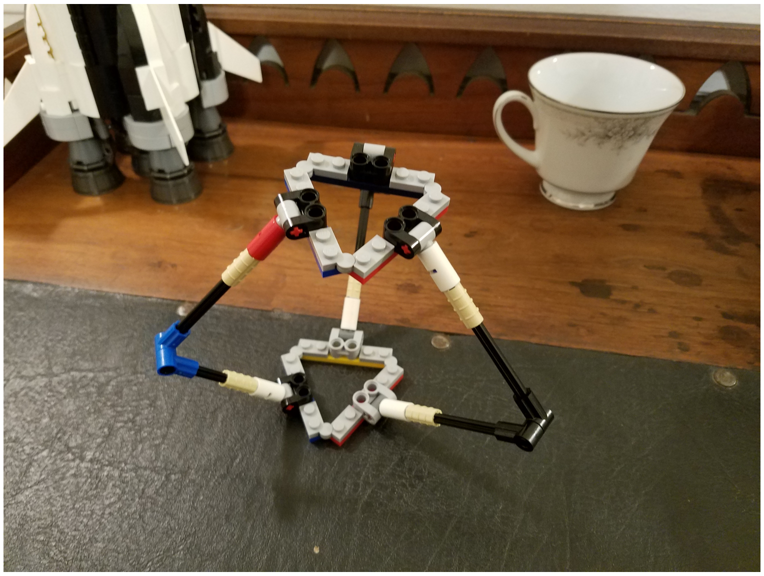

Figure 5.4. LEGO Technics model.

Table 5.2. Bill of materials for LEGO Technics model.

LEGO Part #	**Part Description**	**Quantity**
3666	1x6 Flat	6
43093	Connector Bushing with Friction Cross Axle	6
3706	6 cm Cross Axle	6
15100	Single Bushing - 2 cm, .49 cm diameter	6
19954	1x2 Hinge Plate	6
6538	Ribbed Cross Axle Extension	6
32062	2 cm Cross Axle With Groove	12
32013	Technic 0° Angle Element	6
41678	Technic Cross Block/Fork, 2x2	6
29219	Tube with Double .485 cm Hole	6

5.2 Virtual Model in Geogebra

Geogebra, an open-source program for geometric modeling, was used to produce a 3D model of the analysis in Section 3.2. The model is shown in Figure 5.5, and was used to generate several of the figures herein. It may be accessed at **https://www.geogebra.org/m/jZq4**

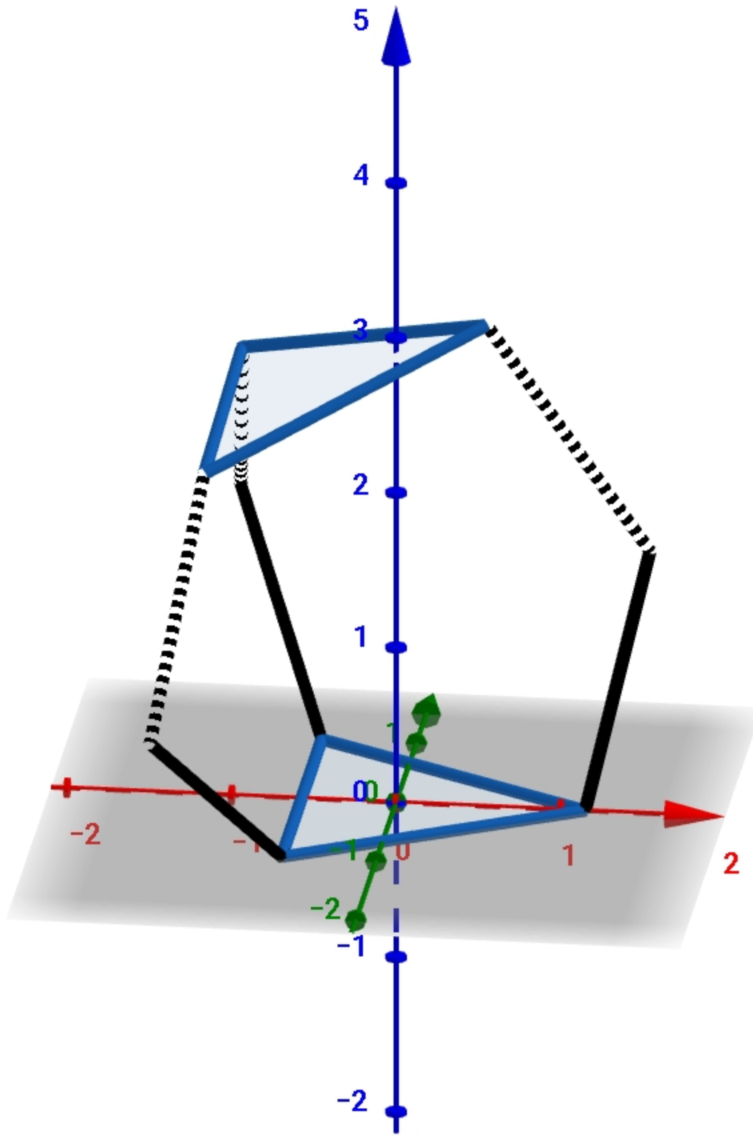

Figure 5.5. Geogebra model of the Canfield joint, with minimal labeling.

5.3 Virtual Model in Gazebo

To facilitate future work, a model of the Canfield joint was created in Simulation Description Format[26] and controlled in Gazebo,[27] a physics simulator, using Robot Operating System[28], a set of open-source libraries for robotics simulation and control.

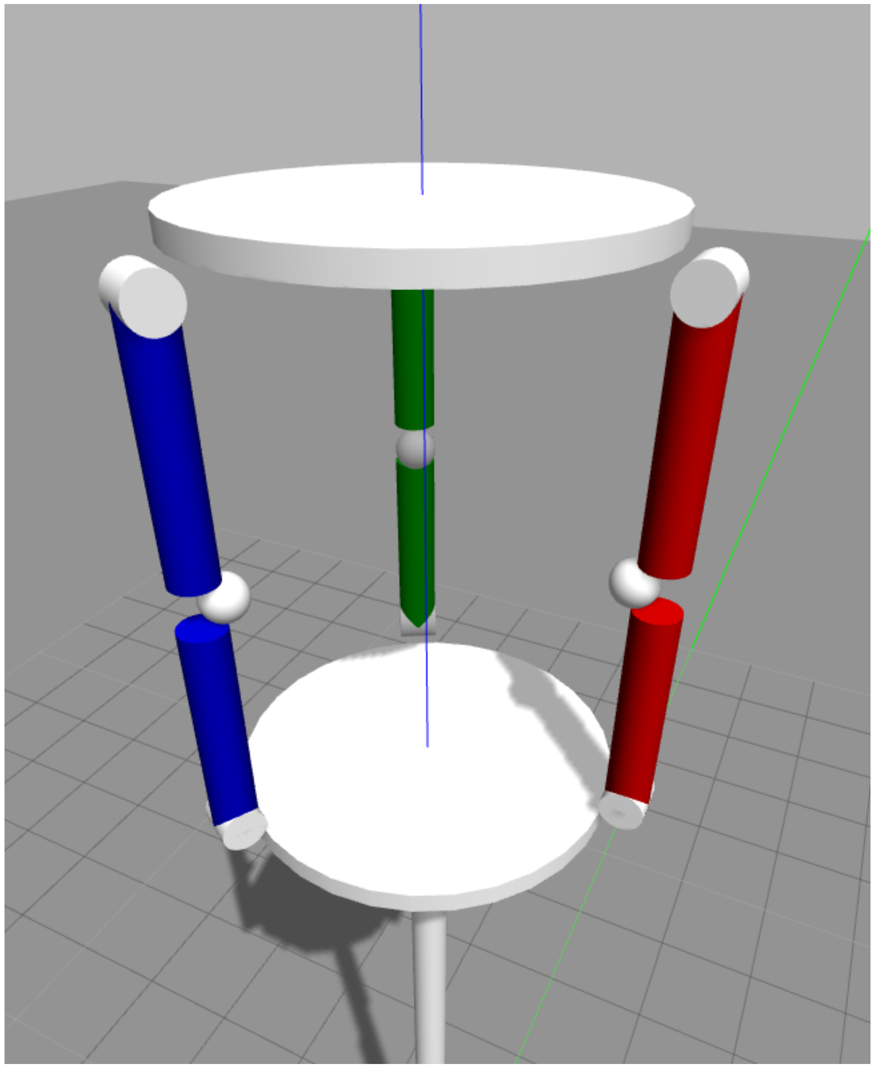

Figure 5.6. Canfield joint model, shown in the Gazebo physics engine.

The model was created in the .sdf format, rather than the .urdf format traditionally used for ROS, because .sdf allows for parallel linkages while .urdf does not. This model, shown in Figure 5.6, may be adapted for specific implementations of the Canfield joint and used as a basis for controlling a physical robot.

5.3.1 Motivation

Robot Operating System (ROS) provides an open-source framework for robotics software development[29]. It is increasing in popularity, and provides a format for standardization such that code from one robotics platform may be adapted freely to others. This allows for modularity in design, since one model may be added onto another. ROS tools include Gazebo, the physics simulator in which the model is tested, and RViz, a 3D visualizer for sensor data. These tools are maintained by the Open Source Robotics Foundation.

5.3.2 Execution

The following instructions may be executed on a computer where ROS Kinetic or Lunar has been installed. The files are available on Github.[30] The SDF model is included in Appendix B.

First, Gazebo is launched with this terminal command;

```
roslaunch gazebo_ros empty_world.launch
```

Gravity may be changed to zero in the left sidebar in Gazebo, or by running the following terminal command:

```
rosservice call /gazebo/set_physics_properties 0.001 1000.0 '
   [0.0, 0.0, 0.0]' '[False, 0, 50, 1.3, 0.0, 0.001, 100.0,
   0.0, 0.2, 20]'
```

This terminal command restores gravity to normal:

```
rosservice call /gazebo/set_physics_properties 0.001 1000.0 '
   [0.0, 0.0, -9.8]' '[False, 0, 50, 1.3, 0.0, 0.001, 100.0,
   0.0, 0.2, 20]'
```

A model can be spawned in Gazebo using the following code. The final string is the label of the model in Gazebo.

```
cd ~/catkin_ws/src

rosrun gazebo_ros spawn_model -file canfield.sdf -sdf -x 0 -y
   0 -z 1 -model Canfield
```

To perturb the model from the command line, run a variant on the line:

```
rosservice call /gazebo/apply_joint_effort joint1 -- 10000 0
   1000000
```

Controller. The controller may be run with a variant on the following line of code:

```
rosrun canfield_joint_controller{,} &
```

6 Conclusions and Future Research

6.1 Achievements

This thesis describes the development and implementation of a metrology platform for the validation of a system for optical pointing, and the partial validation of an existing prototype Canfield joint using that system. It also encompasses a kinematic analysis of the Canfield joint, including previously unknown singularities, and the design and construction of several models for future use. This represents a promising step towards a pointing system suitable for Mars/Earth optical communications tracking.

6.2 Continued Integration Work

The test procedures described in Chapter 4 may be repeated for this prototype and subsequent revisions. The mathematical work discussed in Chapter 3 is far from exhausted, and may be extended to a more complete joint control system. The ROS models developed herein are very basic. However, they may be iterated upon and used as the basis for more realistic models in applied settings. The next step will be to create a ROS node to calculate the forward kinematics and generate joint impulses along some trajectory.

6.3 Proposed Derivative Constructions

During the course of this research, several derivative linkages based on the Canfield have been proposed.

6.3.1 Asymmetric Linkages

One possible derivative construction is an asymmetric Canfield joint, with different lengths of base and distal legs. Varying the base sizes and symmetry also yields new linkages; preliminary observations indicate that increasing the relative size of the distal plate may avoid the "starfish" actuator singularity. Changing these lengths would require significant adjustments to the kinematic analysis.

6.3.2 Compound Linkage

Another possibility currently under review is connecting two or more Canfield joints with the distal plate of one mated to the base plate of another, perhaps using cable-based actuators. This may lead to a larger workspace, or provide a basis for a mobile robot.

6.4 Education and Outreach

The LEGO models developed in Section 5.1 are well-suited to outreach and educational purposes. They have been used with success at an outreach event at the Cleveland Museum of Natural History. The Canfield joint provides a strong motivating example for several basic engineering and robotics concepts, including composing a bill of materials, constructing subassemblies, adding an end effector to a robot manipulator, and the pointing component of optical communication. Further, the geometric analysis in Section 3.2 can be used at the secondary level as a motivating example for geometric concepts including the construction of a plane and the reflection of points across that plane, while optical communications serve as a motivating example for the trigonometry required to calculate subtended angles. The Geogebra model, being freely accessible online, may also be deployed in educational context to provide a quantitative and interactive model with which students may experiment. These models are presented for educational use in a recent NASA publication.[1]

[1]FS-2018-08-054-GRC, appended.

National Aeronautics and
Space Administration

Make your own

CANFIELD JOINT

The Canfield joint is a pointing mechanism that behaves like a wrist. It can be used to point a number of end effectors, including lasers, solar panels, and thrusters.
The joint is controlled by 3 motors, one at the base of each leg - even if one leg freezes, pointing can still be controlled substantially by the other two. You can use the part numbers here to make your own out of LEGO bricks.

Bill of Materials:

3795 18x

11476 6x

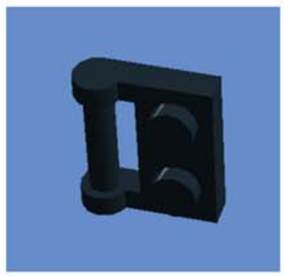

48336 6x

14417 18x

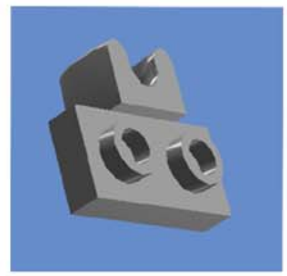

14704 18x

Build two bases:

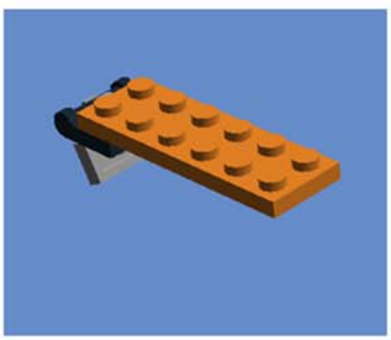

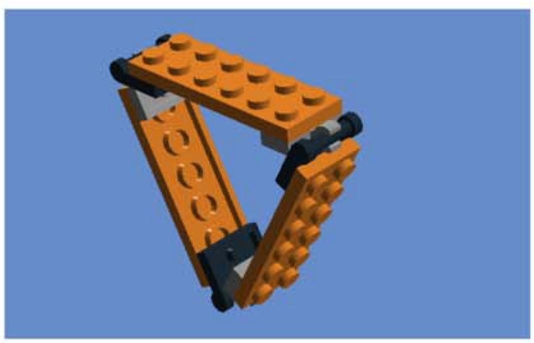

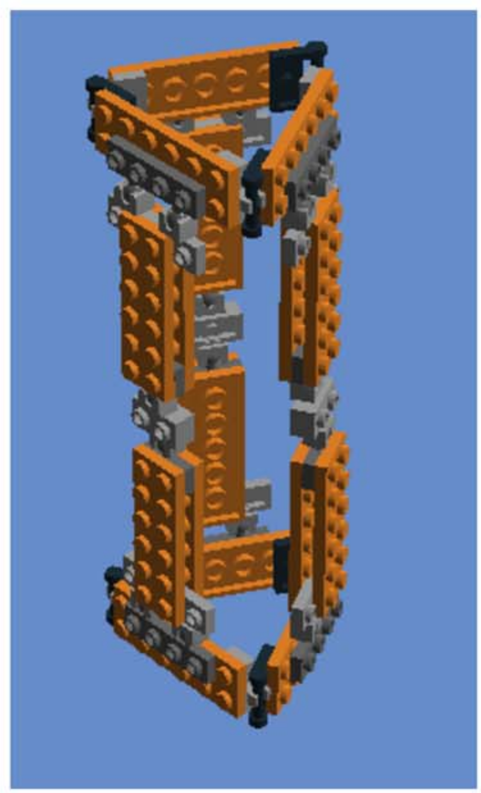

Build three legs:

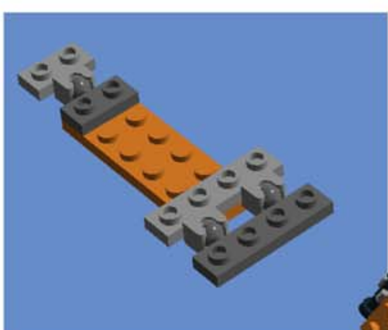

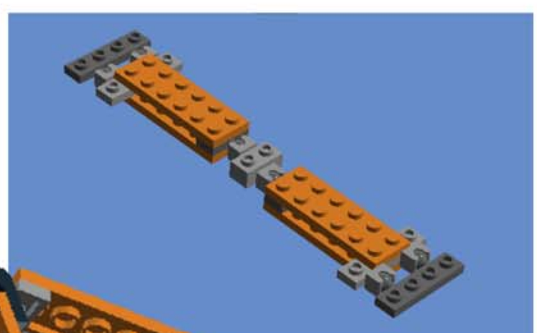

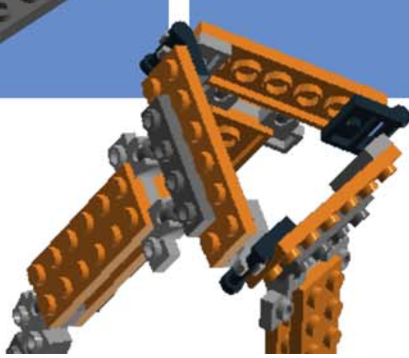

www.nasa.gov

FOR MORE INFORMATION:
www.tiny.cc/iroc
Patent #5699695

Integrated Radio and Optical Communication

APPLICATIONS FOR THE CANFIELD JOINT

Cables can be routed through the center of the Canfield joint to avoid wrapping or tangling, which saves on size, weight, and power (SWaP). Teams at NASA have researched using Canfield joints for thrusters and solar panels. The Integrated Radio and Optical Communication (iROC) project at NASA Glenn is investigating the Canfield joint for precise pointing of lasers in space communication.

SOLAR TRACKING

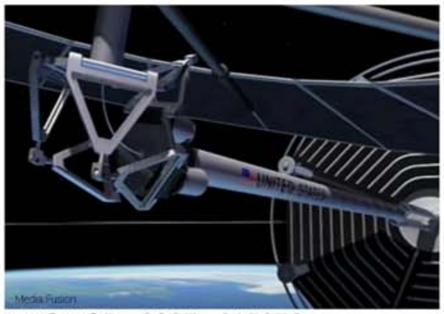

NASA/CR—2007—215076

THRUSTERS

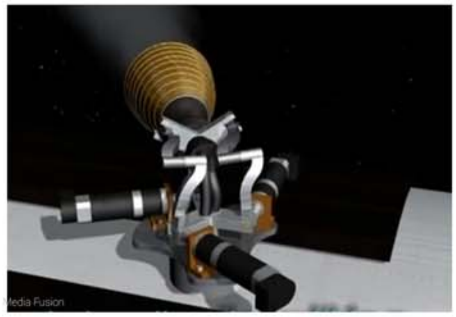

OPTICAL COMMUNICATION

USING GEOMETRY TO DRIVE ROBOTS

Forward kinematics describe how the movement of the base joints affects the position of the top plate. The three elbows define a plane, and then the position of the bottom plate is reflected over that plane to find the position of the top plate. You can simulate your own Canfield joint at **https://ggbm.at/jZq4byKJ**.

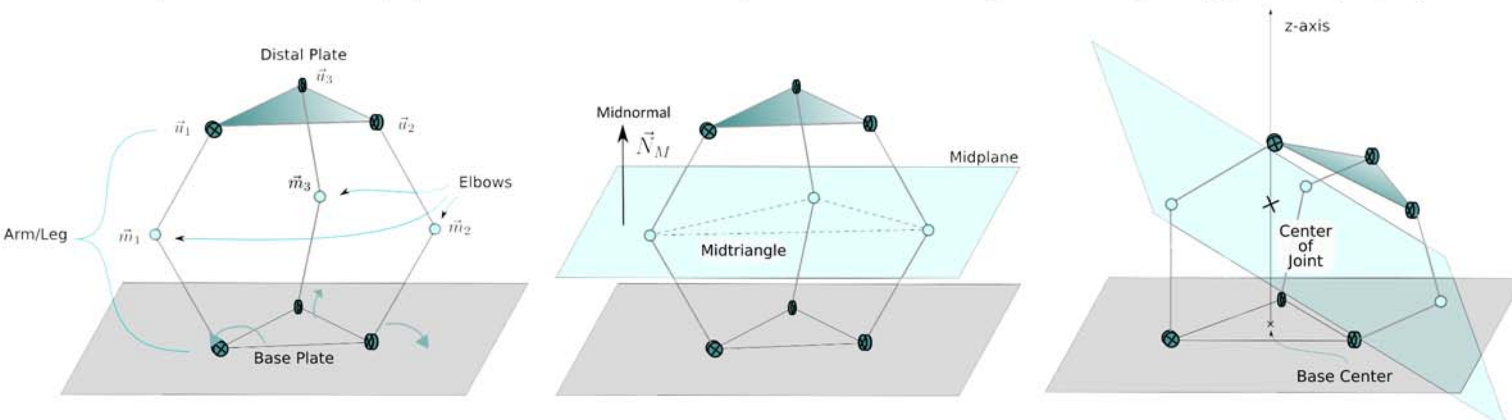

USING TRIGONOMETRY TO EXPLORE SPACE

Laser communication can carry more information than radio, but requires more precise pointing.

Pointing a laser beam from an orbiter around Mars to a ground station on Earth requires a pointing accuracy of 100 microradians, which is roughly the equivalent of pointing at a 1-inch target 300 yards away.

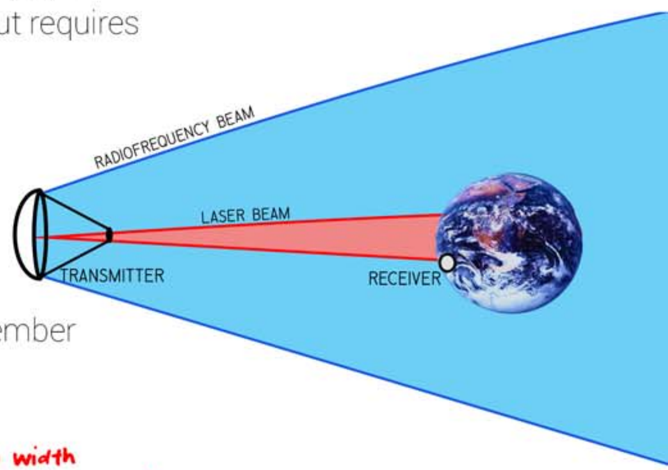

You can calculate the beam width using Heron's formula. Remember that the distance between the planets changes over time.

Subtended Angle

Beam width at Earth

$$\tan\frac{\theta}{2} = \frac{H}{2D}$$

Distance from Earth to Mars

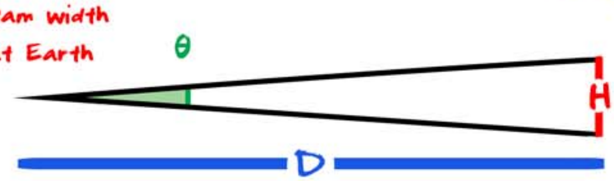

National Aeronautics and Space Administration

Glenn Research Center
21000 Brookpark Road
Cleveland, OH 44106
www.nasa.gov/centers/glenn

www.nasa.gov

FS–2018–08–054–GRC

Appendix A
Validation Code

The following code was used in MATLAB to interface with the KPA101 position aligner using ActiveX controls:

```
actxcontrolselect
fpos    = get(0,'DefaultFigurePosition'); % figure default
    position
fpos(3) = 650; % figure window size;Width
fpos(4) = 450; % Height
f = figure('Position', fpos,...
           'Menu','None',...
           'Name','APT GUI');
h = actxcontrol('APTQUAD.APTQuadCtrl.1', [20 20 600 400 ],
    f)
 %%

h.StartCtrl;
%%
SN = 69250441; %serial number
set(h,'HWSerialNum', SN);
%h.Identify

%%
data=zeros(10000, 4); %preallocation

tic; %timing
for i=1:length(data)
    %pause(.01)
    [a, SumDiff, XDiff, YDiff]=h.ReadSumDiffSignals(0,0,0)
       ;
    %foo=XDiff
    data(i, 1)=toc; %timing
    data(i, 2)= XDiff;
    data(i, 3)= YDiff;
    data(i, 4)= SumDiff;
    i
end
%%
```

```
figure, plot(data(:, 2)), hold on, plot(data(:, 3)), plot(
   data(:, 4)), legend('Xdiff', 'Ydiff', 'Sum')
figure, plot(data(:, 2), 'LineWidth', 2), hold on, plot(
   data(:, 3), 'LineWidth', 2), plot(data(:, 4), '
   LineWidth', 2), legend('Xdiff', 'Ydiff', 'Sum')
```

Appendix B
SDF File

The following code comprises the SDF model of the Canfield joint, written in XML.

```
<sdf version='1.6'>
  <model name='canfield'>
    <self_collide>1</self_collide>
    <link name='pedestal'>
      <pose frame=''>0 0 0 0 -0 0</pose>
      <inertial>
        <pose frame=''>0 0 0 0 -0 0</pose>
        <mass>2</mass>
        <inertia>
          <ixx>6.65125</ixx>
          <ixy>0</ixy>
          <ixz>0</ixz>
          <iyy>6.65125</iyy>
          <iyz>4.44089e-16</iyz>
          <izz>2</izz>
        </inertia>
      </inertial>
      <collision name='arm_collision'>
        <pose frame=''>0.25 0.433 3 0 -0 0</pose>
        <geometry>
          <cylinder>
            <length>6</length>
            <radius>0.1</radius>
          </cylinder>
        </geometry>
      </collision>
      <collision name='
        arm_fixed_joint_lump__base_plate_collision_1'>
        <pose frame=''>0.25 0.433 6.05 0 -0 0</pose>
        <geometry>
          <cylinder>
            <length>0.1</length>
            <radius>0.5</radius>
          </cylinder>
        </geometry>
      </collision>
      <visual name='arm_visual'>
        <pose frame=''>0.25 0.433 3 0 -0 0</pose>
```

```
        <geometry>
          <cylinder>
            <length>6</length>
            <radius>0.1</radius>
          </cylinder>
        </geometry>
      </visual>
      <visual name='arm_fixed_joint_lump__base_plate_visual_1'
         >
        <pose frame=''>0.25 0.433 6.05 0 -0 0</pose>
        <geometry>
          <cylinder>
            <length>0.1</length>
            <radius>0.5</radius>
          </cylinder>
        </geometry>
      </visual>
    </link>


    <joint name='glue_robot_to_world' type='revolute'>
      <child>pedestal</child>
      <parent>world</parent>
      <axis>
        <limit>
          <lower>0</lower>
          <upper>0</upper>
        </limit>
        <dynamics>
          <damping>0</damping>
          <friction>0</friction>
          <spring_reference>0</spring_reference>
          <spring_stiffness>0</spring_stiffness>
        </dynamics>
        <use_parent_model_frame>1</use_parent_model_frame>
        <xyz>0 0 1</xyz>
      </axis>
    </joint>


    <link name='base_leg_1'>

      <pose frame=''>0 0 6.1 0 -0 0</pose>
      <inertial>
        <pose frame=''>0 0 0.5 0 -0 0</pose>
        <mass>1</mass>
```

```
      <inertia>
        <ixx>0.1</ixx>
        <ixy>0</ixy>
        <ixz>0</ixz>
        <iyy>0.1</iyy>
        <iyz>0</iyz>
        <izz>0.005</izz>
      </inertia>
    </inertial>
    <collision name='base_leg_1_collision'>

      <pose frame=''>0 0 0.5 0 -0 0</pose>
      <geometry>
        <cylinder>
          <length>1</length>
          <radius>0.1</radius>
        </cylinder>
      </geometry>
    </collision>
    <visual name='base_leg_1_visual'>
      <pose frame=''>0 0 0.5 0 -0 0</pose>
      <geometry>
        <cylinder>
          <length>1</length>
          <radius>0.1</radius>
        </cylinder>
      </geometry>
        <material>
  <ambient>1 0 0 1</ambient>
  <diffuse>1 0 0 1</diffuse>
  <specular>0.1 0.1 0.1 1</specular>
  <emissive>0 0 0 0</emissive>
</material>
    </visual>
  </link>

  <joint name='joint1' type='revolute'>
    <child>base_leg_1</child>
    <parent>pedestal</parent>
    <axis>
      <xyz>-1 1 0</xyz>
      <limit>
        <lower>-1e+16</lower>
        <upper>1e+16</upper>
      </limit>
      <dynamics>
```

```
        <spring_reference>0</spring_reference>
        <spring_stiffness>0</spring_stiffness>
      </dynamics>
      <use_parent_model_frame>1</use_parent_model_frame>
    </axis>
  </joint>


  <link name='distal_leg_1'>

    <pose frame=''>0 0 7.1 0 -0 0</pose>
    <inertial>
      <pose frame=''>0 0 0.5 0 -0 0</pose>
      <mass>1</mass>
      <inertia>
        <ixx>0.1</ixx>
        <ixy>0</ixy>
        <ixz>0</ixz>
        <iyy>0.1</iyy>
        <iyz>0</iyz>
        <izz>0.005</izz>
      </inertia>
    </inertial>
    <collision name='distal_leg_1_collision'>

      <pose frame=''>0 0 0.5 0 -0 0</pose>
      <geometry>
        <cylinder>
          <length>1</length>
          <radius>0.1</radius>
        </cylinder>
      </geometry>
    </collision>

    <visual name='distal_leg_1_visual'>
      <pose frame=''>0 0 0.5 0 -0 0</pose>
      <geometry>
        <cylinder>
          <length>1</length>
          <radius>0.1</radius>
        </cylinder>
      </geometry>
    </visual>
  </link>
```

```
<joint name='midjoint1' type='ball'>
  <child>distal_leg_1</child>
  <parent>base_leg_1</parent>
  <axis>
    <xyz>0 1 0</xyz>
    <limit>
      <lower>-1e+16</lower>
      <upper>1e+16</upper>
    </limit>
    <dynamics>
      <spring_reference>0</spring_reference>
      <spring_stiffness>0</spring_stiffness>
    </dynamics>
    <use_parent_model_frame>1</use_parent_model_frame>
  </axis>
</joint>


<link name='base_leg_2'>
  <pose frame=''>0 1 6.1 0 -0 0</pose>
  <inertial>
    <pose frame=''>0 0 0.5 0 -0 0</pose>
    <mass>1</mass>
    <inertia>
      <ixx>0.1</ixx>
      <ixy>0</ixy>
      <ixz>0</ixz>
      <iyy>0.1</iyy>
      <iyz>0</iyz>
      <izz>0.005</izz>
    </inertia>
  </inertial>
  <collision name='base_leg_2_collision'>

    <pose frame=''>0 0 0.5 0 -0 0</pose>
    <geometry>
      <cylinder>
        <length>1</length>
        <radius>0.1</radius>
      </cylinder>
    </geometry>
  </collision>
  <visual name='base_leg_2_visual'>
    <pose frame=''>0 0 0.5 0 -0 0</pose>
    <geometry>
      <cylinder>
```

```
          <length>1</length>
          <radius>0.1</radius>
        </cylinder>
      </geometry>
    </visual>
  </link>


  <joint name='joint2' type='revolute'>
    <child>base_leg_2</child>
    <parent>pedestal</parent>
    <axis>
      <xyz>1 1 0</xyz>
      <limit>
        <lower>-1e+16</lower>
        <upper>1e+16</upper>
      </limit>
      <dynamics>
        <spring_reference>0</spring_reference>
        <spring_stiffness>0</spring_stiffness>
      </dynamics>
      <use_parent_model_frame>1</use_parent_model_frame>
    </axis>
  </joint>


  <link name='distal_leg_2'>

    <pose frame=''>0 1 7.1 0 -0 0</pose>
    <inertial>
      <pose frame=''>0 0 0.5 0 -0 0</pose>
      <mass>1</mass>
      <inertia>
        <ixx>0.1</ixx>
        <ixy>0</ixy>
        <ixz>0</ixz>
        <iyy>0.1</iyy>
        <iyz>0</iyz>
        <izz>0.005</izz>
      </inertia>
    </inertial>
    <collision name='distal_leg_2_collision'>

      <pose frame=''>0 0 0.5 0 -0 0</pose>
      <geometry>
        <cylinder>
```

```
          <length>1</length>
          <radius>0.1</radius>
        </cylinder>
      </geometry>
    </collision>
    <visual name='distal_leg_2_visual'>
      <pose frame=''>0 0 0.5 0 -0 0</pose>
      <geometry>
        <cylinder>
          <length>1</length>
          <radius>0.1</radius>
        </cylinder>
      </geometry>
    </visual>
  </link>


  <joint name='midjoint2' type='ball'>
    <child>distal_leg_2</child>
    <parent>base_leg_2</parent>
    <axis>
      <xyz>0 1 0</xyz>
      <limit>
        <lower>-1e+16</lower>
        <upper>1e+16</upper>
      </limit>
      <dynamics>
        <spring_reference>0</spring_reference>
        <spring_stiffness>0</spring_stiffness>
      </dynamics>
      <use_parent_model_frame>1</use_parent_model_frame>
    </axis>
  </joint>


  <link name='distal_plate'>

    <pose frame=''>0 1 8.1 0 -0 0</pose>
    <inertial>
      <pose frame=''>0.3 -0.55 0.05 0 -0 0</pose>
      <mass>1</mass>
      <inertia>
        <ixx>1</ixx>
        <ixy>0</ixy>
        <ixz>0</ixz>
        <iyy>1</iyy>
```

```
        <iyz>0</iyz>
        <izz>1</izz>
      </inertia>
    </inertial>
    <collision name='distal_plate_collision'>

      <pose frame=''>0.3 -0.55 0.05 0 -0 0</pose>
      <geometry>
        <cylinder>
          <length>0.1</length>
          <radius>0.5</radius>
        </cylinder>
      </geometry>
    </collision>
    <visual name='distal_plate_visual'>
      <pose frame=''>0.3 -0.55 0.05 0 -0 0</pose>
      <geometry>
        <cylinder>
          <length>0.1</length>
          <radius>0.5</radius>
        </cylinder>
      </geometry>
    </visual>
  </link>


   <link name='base_leg_3'>

    <pose frame=''>0.866 0.5 6.1 0 -0 0</pose>
    <inertial>
      <pose frame=''>0 0 0.5 0 -0 0</pose>
      <mass>1</mass>
      <inertia>
        <ixx>0.1</ixx>
        <ixy>0</ixy>
        <ixz>0</ixz>
        <iyy>0.1</iyy>
        <iyz>0</iyz>
        <izz>0.005</izz>
      </inertia>
    </inertial>
    <collision name='base_leg_3_collision'>

      <pose frame=''>0 0 0.5 0 -0 0</pose>
      <geometry>
        <cylinder>
```

```
          <length>1</length>
          <radius>0.1</radius>
        </cylinder>
      </geometry>
    </collision>
    <visual name='base_leg_3_visual'>
      <pose frame=''>0 0 0.5 0 -0 0</pose>
      <geometry>
        <cylinder>
          <length>1</length>
          <radius>0.1</radius>
        </cylinder>
      </geometry>
    </visual>
  </link>


  <joint name='joint3' type='revolute'>
    <child>base_leg_3</child>
    <parent>pedestal</parent>
    <axis>
      <xyz>0 1 0</xyz>
      <limit>
        <lower>-1e+16</lower>
        <upper>1e+16</upper>
      </limit>
      <dynamics>
        <spring_reference>0</spring_reference>
        <spring_stiffness>0</spring_stiffness>
      </dynamics>
      <use_parent_model_frame>1</use_parent_model_frame>
    </axis>
  </joint>


  <link name='distal_leg_3'>

    <pose frame=''>0.866 0.5 7.1 0 -0 0</pose>
    <inertial>
      <pose frame=''>0 0 0.5 0 -0 0</pose>
      <mass>1</mass>
      <inertia>
        <ixx>0.1</ixx>
        <ixy>0</ixy>
        <ixz>0</ixz>
        <iyy>0.1</iyy>
```

```
       <iyz>0</iyz>
       <izz>0.005</izz>
     </inertia>
   </inertial>
   <collision name='distal_leg_3_collision'>

     <pose frame=''>0 0 0.5 0 -0 0</pose>
     <geometry>
       <cylinder>
         <length>1</length>
         <radius>0.1</radius>
       </cylinder>
     </geometry>
   </collision>
   <visual name='distal_leg_3_visual'>
     <pose frame=''>0 0 0.5 0 -0 0</pose>
     <geometry>
       <cylinder>
         <length>1</length>
         <radius>0.1</radius>
       </cylinder>
     </geometry>
   </visual>
 </link>


 <joint name='midjoint3' type='ball'>
   <child>distal_leg_3</child>
   <parent>base_leg_3</parent>
   <axis>
     <xyz>0 1 0</xyz>
     <limit>
       <lower>-1e+16</lower>
       <upper>1e+16</upper>
     </limit>
     <dynamics>
       <spring_reference>0</spring_reference>
       <spring_stiffness>0</spring_stiffness>
     </dynamics>
     <use_parent_model_frame>1</use_parent_model_frame>
   </axis>
 </joint>


<joint name='distal_joint2' type='revolute'>
   <child>distal_plate</child>
```

```
    <parent>distal_leg_2</parent>
    <axis>
      <xyz>1 1 0</xyz>
      <limit>
        <lower>-1e+16</lower>
        <upper>1e+16</upper>
      </limit>
      <dynamics>
        <spring_reference>0</spring_reference>
        <spring_stiffness>0</spring_stiffness>
      </dynamics>
      <use_parent_model_frame>1</use_parent_model_frame>
    </axis>
  </joint>


  <joint name='distal_joint1' type='revolute'>
    <child>distal_plate</child>
    <parent>distal_leg_1</parent>
    <axis>
      <xyz>0 -1 0</xyz>
      <limit>
        <lower>-1e+16</lower>
        <upper>1e+16</upper>
      </limit>
      <dynamics>
        <spring_reference>0</spring_reference>
        <spring_stiffness>0</spring_stiffness>
      </dynamics>
      <use_parent_model_frame>1</use_parent_model_frame>
    </axis>
  </joint>




  <joint name='distal_joint3' type='revolute'>
    <child>distal_plate</child>
    <parent>distal_leg_3</parent>
      <axis>
      <xyz>1 -1 0</xyz>
      <limit>
        <lower>-1e+16</lower>
        <upper>1e+16</upper>
      </limit>
      <dynamics>
```

```
          <spring_reference>0</spring_reference>
          <spring_stiffness>0</spring_stiffness>
        </dynamics>
        <use_parent_model_frame>1</use_parent_model_frame>
      </axis>
    </joint>


  </model>
</sdf>
```

Complete References

[1] Tony Nerone Jim Budinger. iROC Gimbal Data for Meeting with Moog Corporation, November 5 2014.

[2] Willard Pollard. Position-controlling apparatus, June 16 1942. US Patent 2,286,571.

[3] keuwlsoft. Accelerometer meter. URL: http://www.keuwl.com/Accelerometer/.

[4] Daniel Raible. Space Communications, 2015. URL: https://www.youtube.com/watch?v=iOrSlNm-SCY.

[5] Devi Chadha. Terrestrial Wireless Optical Communication. McGraw-Hill Education, 2013.

[6] Stephen L. Canfield and Charles F. Reinholtz. Development of the carpal robotic wrist, pages 423–434. Springer Berlin Heidelberg, Berlin, Heidelberg, 1998.

[7] Thuy Mai. Technology Readiness Level, 2012. URL: https://www.nasa.gov/directorates/heo/scan/engineering/technology/txt$_{a}ccordion1.html$.

[8] David Whitehead and P. H. Blyth. Athenaeus Mechanicus, On Machines: Translated with Introduction and Commentary (Historia: Einzelschriften) (German Edition). Franz Steiner Verlag, 2004.

[9] Ilian Bonev. The True Origins of Parallel Robots.

[10] J.-P. Merlet. Parallel Robots (Solid Mechanics and Its Applications, 74). Springer, 2000.

[11] Hagay Bamberger. Kinematics of Micro Parallel Robots: Research on MEMS Kinematics. VDM Verlag, 2009.

[12] S.L. Canfield, C.F. Reinholtz, R.J. Salerno, and A.J. Ganino. Spatial, parallel-architecture robotic carpal wrist, December 23 1997. US Patent 5,699,695.

[13] Kirk Sorensen. Steve Canfield and his marvellous mechanical joint, 2010. URL: http://selenianboondocks.com/2010/06/cjoint1/.

[14] Tennessee Tech News. NASA proposes to use Canfield invention in new spacecraft, 2006. URL: https://www.tntech.edu/news/archive/nasa-proposes-to-use-canfield-invention-in-new-spacecraft.

[15] S.L. Canfield. Developing Capture Mechanisms and High-Fidelity Dynamic Models for the MXER Tether System, 2007. NTRS 20080002099.

[16] David G. Aviv. Laser Space Communications (Artech House Space Technology and Applications). Artech House, 2006.

[17] L.W. Tsai. Systematic enumeration of parallel manipulators. In Parallel Kinematic Machines: Theoretical Aspects and Industrial Requirements (Advanced Manufacturing). Springer, 1999.

[18] Richard M. Murray, Zexiang Li, and S. Shankar Sastry. A Mathematical Introduction to Robotic Manipulation. CRC Press Inc, 2013.

[19] Robert Short. A Failure Mode and Singularity Analysis for the Canfield Joint. Unpublished, 2017.

[20] Christian Bueno. The Algebra and Geometry of the Canfield Joint. Unpublished, 2017.

[21] K. Wohlhart. Kinematotropic Linkages, pages 359–368. Springer Netherlands, Dordrecht, 1996.

[22] Anthony Ganino. Mechanical design of the carpal wrist :a parallel-actuated, singularity-free robotic wrist, 2003.

[23] Sebastian Thrun, Wolfram Burgard, and Dieter Fox. Probabilistic Robotics (Intelligent Robotics and Autonomous Agents series). The MIT Press, 2005.

[24] Howie Choset, Kevin M. Lynch, Seth Hutchinson, George A. Kantor, Wolfram Burgard, Lydia E. Kavraki, and Sebastian Thrun. Principles of Robot Motion: Theory, Algorithms, and Implementations (Intelligent Robotics and Autonomous Agents series). A Bradford Book, 2005.

[25] SOAP Report Data for iROC Transit. Unpublished, 2013.

[26] Open Source Robotics Foundation. Simulation Description Format. URL: sdformat.org.

[27] Open Source Robotics Foundation. Gazebo. URL: gazebosim.org.

[28] Open Source Robotics Foundation. Robot Operating System. URL: ros.org.

[29] Wyatt Newman. A Systematic Approach to Learning Robot Programming with ROS. Chapman and Hall/CRC, 2017.

[30] K. Collins. Github. https://github.com/KCollins/Canfield.